NUREG/CR-1164
ANL-79-81

NUREG/CR-1164
ANL-79-81

LIGHT-WATER-REACTOR SAFETY RESEARCH PROGRAM: QUARTERLY PROGRESS REPORT

April--June 1979

ARGONNE NATIONAL LABORATORY, ARGONNE, ILLINOIS

Prepared for the Office of Nuclear Regulatory Research
U. S. NUCLEAR REGULATORY COMMISSION

The facilities of Argonne National Laboratory are owned by the United States Government. Under the terms of a contract (W-31-109-Eng-38) among the U. S. Department of Energy, Argonne Universities Association and The University of Chicago, the University employs the staff and operates the Laboratory in accordance with policies and programs formulated, approved and reviewed by the Association.

MEMBERS OF ARGONNE UNIVERSITIES ASSOCIATION

The University of Arizona
Carnegie-Mellon University
Case Western Reserve University
The University of Chicago
University of Cincinnati
Illinois Institute of Technology
University of Illinois
Indiana University
The University of Iowa
Iowa State University
The University of Kansas
Kansas State University
Loyola University of Chicago
Marquette University
The University of Michigan
Michigan State University
University of Minnesota
University of Missouri
Northwestern University
University of Notre Dame
The Ohio State University
Ohio University
The Pennsylvania State University
Purdue University
Saint Louis University
Southern Illinois University
The University of Texas at Austin
Washington University
Wayne State University
The University of Wisconsin-Madison

Available from

GPO Sales Program
Division of Technical Information and Document Control
U. S. Nuclear Regulatory Commission
Washington, D.C. 20555

and

National Technical Information Service
Springfield, Virginia 22161

NUREG/CR-1164
ANL-79-81

(Distribution Codes:
R2, R3, R4)

ARGONNE NATIONAL LABORATORY
9700 South Cass Avenue
Argonne, Illinois 60439

LIGHT-WATER-REACTOR SAFETY RESEARCH PROGRAM: QUARTERLY PROGRESS REPORT
April–June 1979

E. Gale Pewitt, Acting Laboratory Director
Jack A. Kyger, Associate Laboratory Director

Date Published: November 1979

Previous reports in this series

ANL-78-77	April–June 1978
ANL-78-107	July–September 1978
ANL-79-18	October–December 1978
ANL-79-43	January–March 1979

Prepared for the Division of Reactor Safety Research
Office of Nuclear Regulatory Research
U. S. Nuclear Regulatory Commission
Washington, D.C. 20555
Under Interagency Agreement DOE 40-550-75
NRC FIN Nos. A2014, A2016, A2017, A2026

ABSTRACT

This progress report summarizes the Argonne National Laboratory work performed during April, May, and June 1979 on water-reactor-safety problems. The following research and development areas are covered: (1) Loss-of-coolant Accident Research: Heat Transfer and Fluid Dynamics; (2) Transient Fuel Response and Fission-product Release Program; and (3) Mechanical Properties of Zircaloy Containing Oxygen.

NRC FIN No.	FIN Title
A2014	Heat Transfer Coordination for LOCA Research Programs
A2016	Transient Fuel Response and Fission-product Release
A2017	Mechanical Properties of Zircaloy
A2026	Phenomenological Modeling and Experiments in Water Reactor Safety

TABLE OF CONTENTS

	Page
I. LOSS-OF-COOLANT ACCIDENT RESEARCH: HEAT TRANSFER AND FLUID DYNAMICS	1
A. Transient Critical Heat Flux	1
1. Further Verification of Transient Thermal-Hydraulic Code	1
2. Transient CHF Analysis	3
a. Moxon-Edwards Data	3
b. Roumy's Data	5
c. Data of Cumo et al.	6
d. ANL Flow Transients	6
e. ANL Combined Flow and Pressure Transients	8
References	9
II. TRANSIENT FUEL RESPONSE AND FISSION-PRODUCT RELEASE PROGRAM	11
A. Introduction and Summary	11
B. Modeling of Fuel/Fission-product Behavior	11
1. High-burnup Fission-gas Release	11
a. Introduction	11
b. Paths for Fission-gas Release	12
C. Bubble Diffusivities and Gas-atom Re-solution	13
D. Gas-bubble Swelling, Grain-edge Porosity Interconnection, and Grain-boundary Separation	14
E. Fission-gas Bubble Mobilities during Transient Heating and the Prediction of Fission-gas Behavior under Normal Irradiation Conditions	15
F. High-burnup Fission-gas-release Predictions	18
G. Experimental Program	19
1. Replacement DEH Chamber	19
References	20
III. MECHANICAL PROPERTIES OF ZIRCALOY	21
A. Summary	21

TABLE OF CONTENTS

	Page
B. Diametral Tube-compression Properties of Ruptured Zircaloy-4 Cladding	21
C. Tensile Properties of Zircaloy-4 Cladding after Rupture and Oxidation in Steam	26
D. Tabulation of Impact, Diametral Tube-compression, and Tensile Data for Ruptured Zircaloy-4 Cladding	28
E. Recommended Zircaloy Embrittlement Criteria Based upon the Results of This Investigation	28
References	34

I. LOSS-OF-COOLANT ACCIDENT RESEARCH: HEAT TRANSFER AND FLUID DYNAMICS

Responsible Section Managers:
H. K. Fauske, R. D. Henry, and P. A. Lottes, RAS

A. Transient Critical Heat Flux (J. C. M. Leung and K. A. Gallivan, RAS)

1. Further Verification of Transient Thermal-Hydraulic Code

The present scheme, named CODA, which neglects the acoustic phenomena as in COBRA-IV-1,[1] assumes that density (ρ) can be evaluated as a function of enthalpy (h) only. Essentially, this assumption decouples the momentum equation from the continuity and energy equations. Currently, homogeneous equilibrium flow is assumed, which is a valid approximation, particularly for high-pressure systems such as PWR's, and an integral momentum equation is used,[2]

$$\frac{d\bar{G}}{dt} = \frac{1}{L}(\Delta P - F), \tag{1}$$

where

$$\bar{G} = \frac{1}{L}\int_0^L G\, dz,$$

$$F = \left(\frac{G^2}{\rho}\right)_{out} - \left(\frac{G^2}{\rho}\right)_{in} + \int_0^L \frac{2f}{D\rho} G|G|dz + \int_0^L \rho g\, dz,$$

and the other variables have the usual meaning. This technique implies that pressure is eliminated as an unknown in the momentum equation and is simply integrated across specified volume boundaries. The continuity and energy equations are written as

$$\frac{\partial \rho}{\partial t} + \frac{\partial G}{\partial z} = 0 \tag{2}$$

and

$$\frac{\partial h}{\partial t} + \frac{G}{\rho}\frac{\partial h}{\partial z} = \frac{\varphi P_h}{\rho A_x} + \frac{1}{\rho}\frac{\partial P}{\partial t}. \tag{3}$$

The finite-difference forms of Eqs. 1-3 were integrated in stepwise manner using a predictor-corrector scheme.

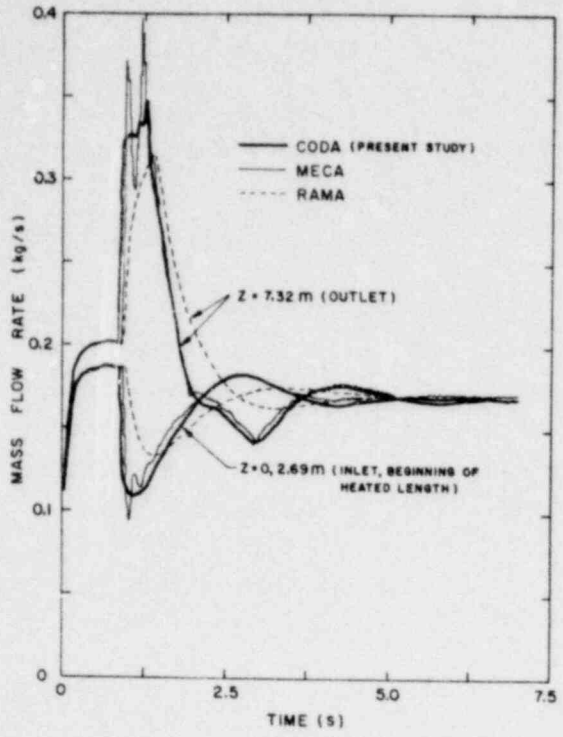

Fig. I.1. Comparison of Mass Flow Rate for Hancox Problem. ANL Neg. No. 900-79-367.

The present scheme is compared against two existing codes as a further verification run. The standard test problem No. 1 as proposed by Hancox and Banerjee[3] considers an instantaneous heat addition to water flowing in a long pipe. Inlet and exit pressures are fixed at 7.102 and 6.984 MPa, respectively, during the transient. The results of CODA are compared with MECA,[4] a method of characteristics procedure, and RAMA,[3] a characteristic finite-difference scheme. Figure I.1 shows close agreement in predicted mass flow rate between CODA and MECA, whereas RAMA appears to smear out much of the detailed features of the solution. CODA predicts a slightly lower steady-state mass flow rate beyond 5 s, and this is felt to be caused by the use of a constant friction factor[5] for the two-phase fluid (f = 0.005) in CODA as opposed to the more complicated formula in MECA and RAMA codes.[3] Figure I.2 shows good agreement in enthalpy history between CODA and MECA; the slightly higher exit enthalpy beyond 5 s in CODA is a direct result of the smaller predicted mass flow.

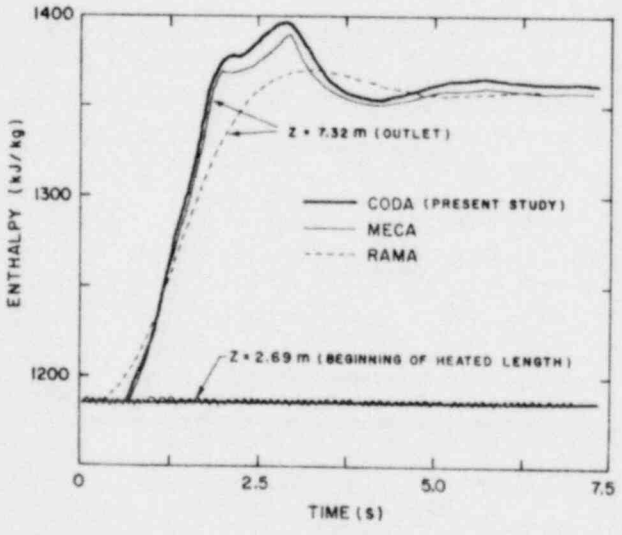

Fig. I.2

Comparison of Enthalpy for Hancox Problem. ANL Neg. No. 900-79-369.

In conclusion, the present scheme has been demonstrated to be comparable to existing codes, but presents itself as a simpler and efficient tool in the analysis of safety experiments.

2. Transient CHF Analysis

The capability of the present code in predicting dryout onset during a flow transient is demonstrated in this section. Transient data are selected based on their availability of information, and the four sets chosen in the present study are described in Table I.1. All the test sections are of round-tube geometry with both uniform and nonuniform axial heat flux, and each set of data is analyzed separately below.

TABLE I.1. Test Conditions for Flow Transient

Ref.	Investigators (Laboratory)	Fluid	Test-section Geometry	Pressure, MPa	Transient Type
6	Moxon & Edwards (AEEW)	Water	Tube ID = 10.8 mm L = 3.66 m	6.9	Rapid exponential flow decay at constant pressure
7	Roumy (CENG)	Water	Tube ID = 10 mm, L = 1.0 m; ID = 6 mm, L = 1.5 m.	14.0	Flow halfing in 0.5 s at constant pressure.
8	Cumo (CNEN)	Freon-12	Tube ID = 7.8 mm, L = 2.0 m	1.0, 1.8	Exponential flow decay at constant pressure.
-	Leung (ANL)	Freon-11	Tube ID = 11.7 mm L = 2.75 m		
			Uniform flux	2.1, 2.9	Linear flow decay at 4%/s, with varying system pressure.
			Outlet peaking	2.1	Inlet-flow blockage
			Chopped-cosine & inlet peaking	2.1	Inlet-flow blockage with system depressurization.

a. Moxon-Edwards Data[6]

Twelve tests were conducted with an inlet exponential flow decay that can be represented by the equation

$$G_{in} = 786 + 1926e^{-3.64t} \text{ kg/m}^2\cdot\text{s} \quad (4)$$

The onset of dryout was always detected at the exit by the three-wire thermocouples. Figure I.3 compares the actual inlet velocity and the assumed inlet velocity of Eq. 4, and the calculated exit velocity using the CODA (present study) and SLIP code.[9] Agreement in the latter is satisfactory. Three steady-state CHF correlations, namely, Bowring,[10] Biasi et al.,[11] and CISE,[12] are used with the calculated local mass velocity and quality to predict when and where dryout onset would occur. The result is shown in Fig. I.4, where Bowring's correlation gives the best agreement in the dryout times. Using the Biasi correlation tends to overestimate the dryout time, whereas using the CISE correlation yields the opposite trend. The prediction performed by Whalley et al.[13] using the Harwell annular-flow dryout model[14] is also shown in Fig. I.4, and it is interesting to note that Harwell's prediction is close to the CISE correlation and that both predict dryout times too early in the transient.

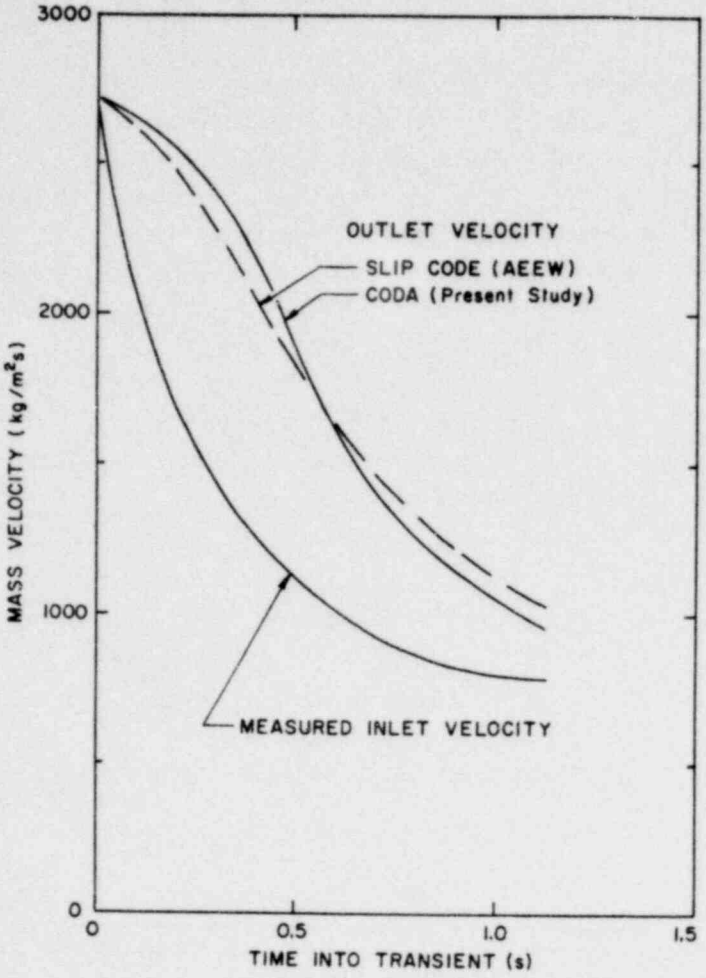

Fig. I.3

Flow-transient History of Moxon-Edwards Run 45/275. ANL Neg. No. 900-79-636.

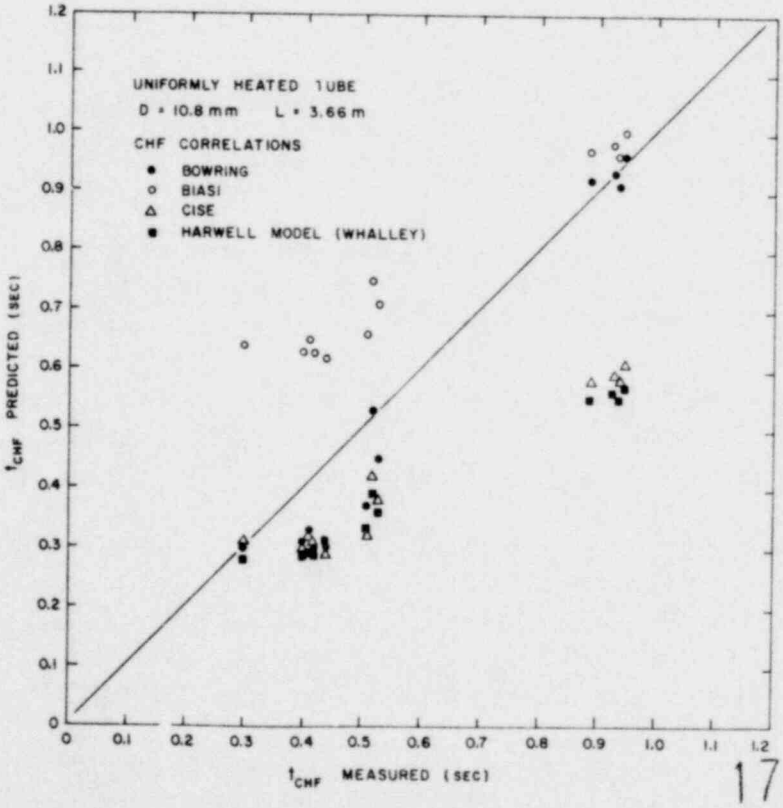

Fig. I.4

Results of CHF Prediction for Moxon-Edwards Data. ANL Neg. No. 900-79-366.

b. Roumy's Data[7]

Only two transient tests conducted at 14 MPa are reported, and the predicted dryout times for the first test (27.3.1.2) using the Bowring, Biasi et al., and CISE correlations are 0.79, 0.84, and 0.74 s, respectively, whereas experimentally dryout was measured near the exit at 0.84 s. However, for the second test, which was conducted in a different test section, the measured CHF at 0.97 s was not predicted at all by any of the three correlations. The critical-heat-flux ratio (CHFR = CHF/local heat flux) is shown in Fig. I.5 as a function of time, and the Bowring correlation gives a CHFR value of 1.14 at the moment of observed CHF, while the other two correlations yield even higher values.

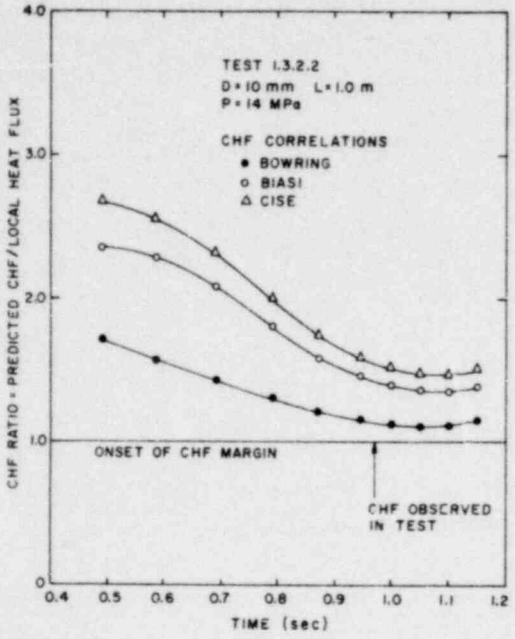

Fig. I.5. CHF Approach in Roumy Flow Transient. ANL Neg. No. 900-79-623.

It is of significance to compare the reported steady-state CHF data obtained in this test section with the CHF correlations. The result is shown in Fig. I.6 for a mass velocity of 1500 kg/m^2·s. All the correlations overpredict CHF values, and at quality of about zero, Bowring's correlation overestimates by about 17%. The calculated exit fluid conditions at measured CHF onset are: mass velocity of 1200 kg/m^2·s and quality of 0.02. The incapability of predicting a CHF in this test is felt to be a result of discrepancy in correlating the steady-state CHF data with the chosen correlations.

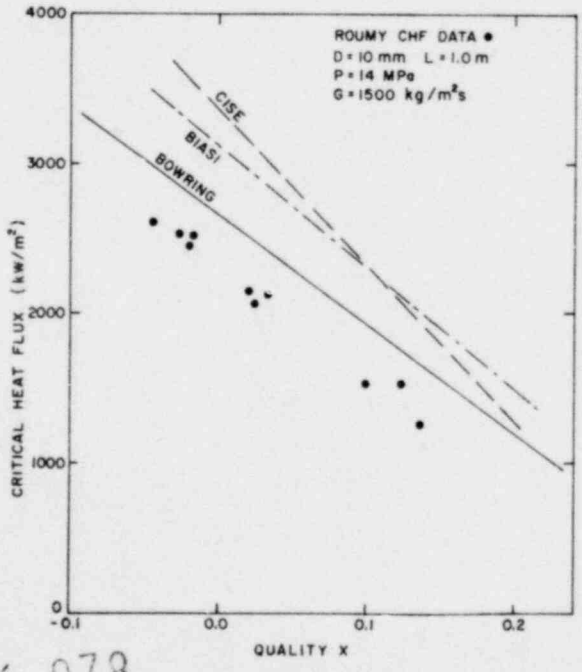

Fig. I.6
Steady-state CHF Data of Roumy. ANL Neg. No. 900-79-622.

c. Data of Cumo et al.[8]

Cumo et al. reported about 150 tests for exponential flow decay at equivalent BWR and PWR pressures in a Freon-12 system. Steady-state CHF data were demonstrated to be well-correlated using the CISE-CNEN Freon correlation;[15] hence this correlation is used to predict dryout onset during the transient. Only the first 10 tests have been analyzed, the results being shown in Fig. I.7. In general, good agreement is obtained for dryout times ranging from about 1 to 12 s.

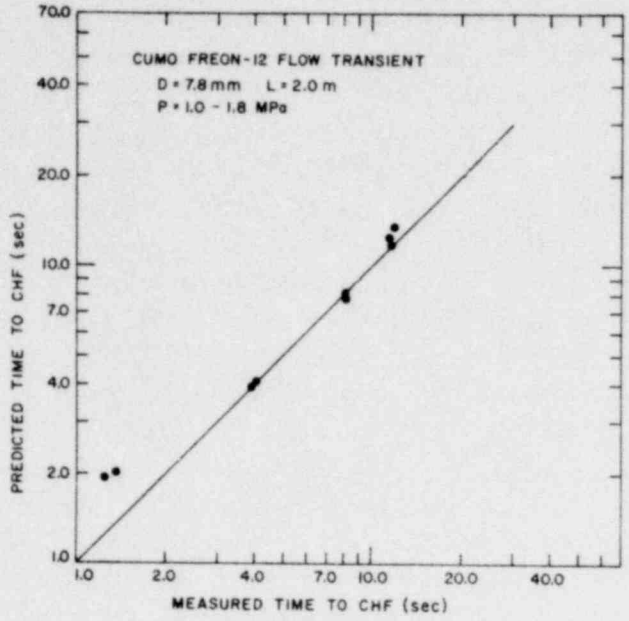

Fig. I.7. Results of CHF Prediction for Cumo's Data. ANL Neg. No. 900-79-592.

d. ANL Flow Transients

The first series consists of fifteen 4%/s flow-coastdown tests, which were intended to simulate reactor-coolant-system pump-trip accidents. Power remained constant to the uniformly heated tube during the transient until being tripped by an overheating protective circuit. Again the CISE Freon correlation has been shown to correlate the steady-state CHF data well. Figure I.8 shows the results using the local-condition CHF prediction. The predicted times appear to be slightly conservative, on

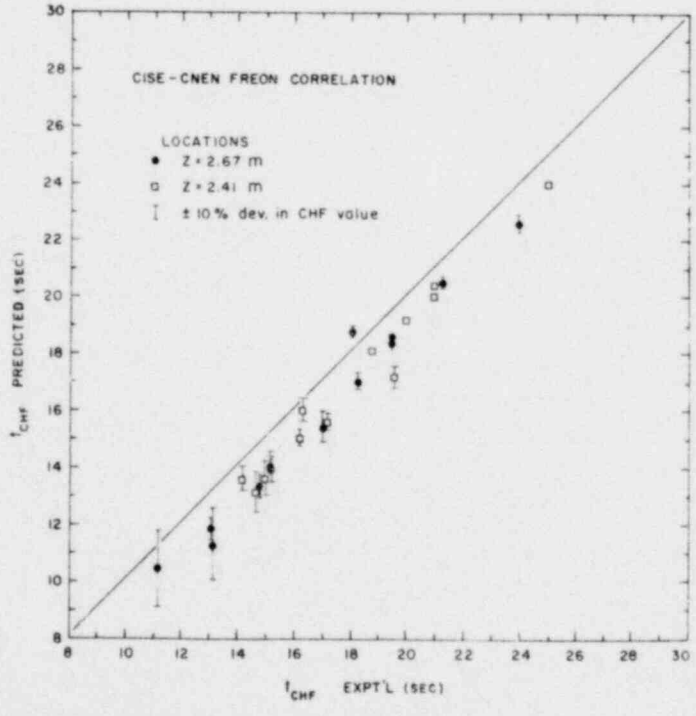

Fig. I.8

Prediction of CHF Using Local-condition Hypothesis in 4%/s Flow-decay Tests. ANL Neg. No. 900-79-372.

the order of 1 s. Another well-known CHF hypothesis is the boiling-length or hydrodynamic-condition hypothesis,

$$q_{CHF} = x(L_b, G, P), \tag{5}$$

where L_b is the boiling length. This hypothesis has been shown to yield a better prediction of steady-state CHF data than the local-condition hypothesis[16,17] for nonuniform heat-flux data. In the present prediction of transient CHF, the boiling length is taken to be the instantaneous, saturated two-phase region in the tube. The results of the boiling-length analysis are shown in Fig. I.9, where better agreement is observed.

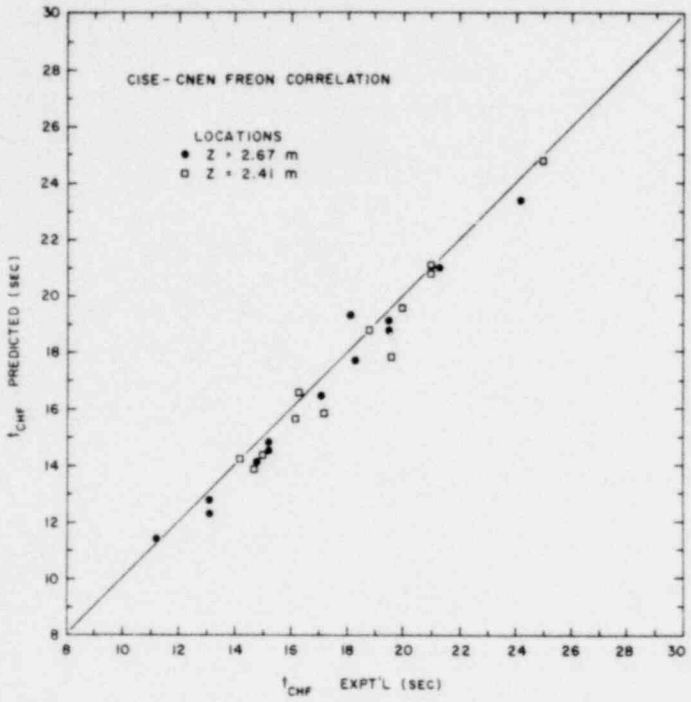

Fig. I.9. Prediction of CHF Using Boiling-length Hypothesis in 4%/s Flow-decay Tests. ANL Neg. No. 900-79-373.

The second series consists of five inlet-flow blockage experiments conducted in an outlet-peaking test section. Table I.2 lists the measured times to CHF at the last three heat-flux zones as well as the predicted times using both hypotheses. Note that dryout occurred first in the next to the last zone (Zone D), and this is predicted by the local-condition hypothesis to within ±0.3 s. The boiling-length hypothesis, however, predicts dryout to occur first nearest to the outlet and then to propagate upstream. Therefore the use of the local-condition hypothesis in this case leads to a better prediction in terms of times to CHF and its propagation. The results are summarized graphically in Fig. I.10.

TABLE I.2. Comparison of Time to CHF for Flow Transients in an Outlet-peaking Test Section

	Zone C			Zone D			Zone E		
z, m	2.36			2.57			2.67		
$\varphi/\bar{\varphi}$	1.35			1.16			0.81		
	t_{CHF}, s								
Run ID	EXP	LC	BL	EXP	LC	BL	EXP	LC	BL
4231	4.3	4.0	4.6	3.7	3.6	4.0	4.6	3.9	3.9
4232	3.5	3.3	3.7	2.8	3.0	3.4	3.9	3.2	3.2
4241	4.9	4.9	>5.0	4.2	4.3	4.8	5.1	4.4	4.6
4242	3.4	3.8	>4.0	2.3	2.6	3.4	2.6	2.8	3.2
4243	1.9	1.8	2.6	1.4	1.2	1.6	1.8	1.5	1.5

Note: $\varphi/\bar{\varphi}$ = local heat flux to average heat flux; EXP = experimental measurement; LC = local-condition prediction; and BL = boiling-length prediction.

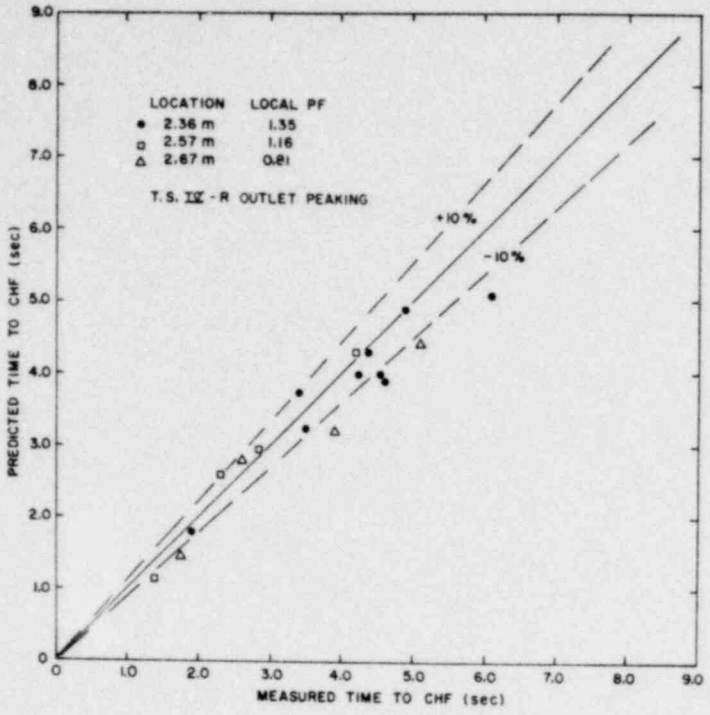

Fig. I.10

Prediction of CHF Using Local-condition Hypothesis in Inlet-flow Stoppage Tests. ANL Neg. No. 900-79-575.

e. ANL Combined Flow and Pressure Transients

Exit-break blowdown experiments are conducted in both chopped-cosine and inlet-peaking heat-flux test sections. The rapid depressurization of the heated section is accompanied by an inlet-flow stoppage under constant power input. The prediction of CHF using the local-condition hypothesis for Tests DB-170 and -315 is shown in Figs. I.11 and I.12, respectively. In general, good agreement is obtained.

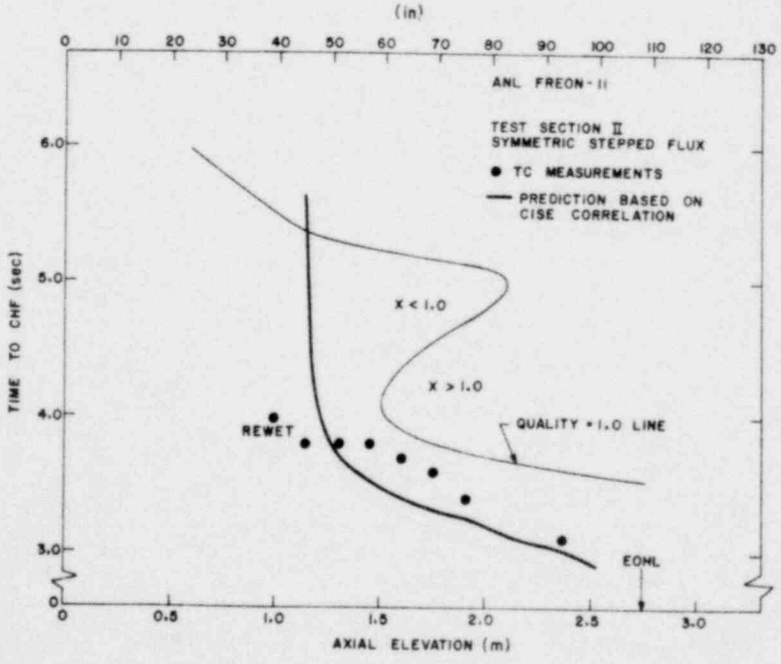

Fig. I.11

Prediction of CHF during Outlet Break Test DB-170. ANL Neg. No. 900-79-586.

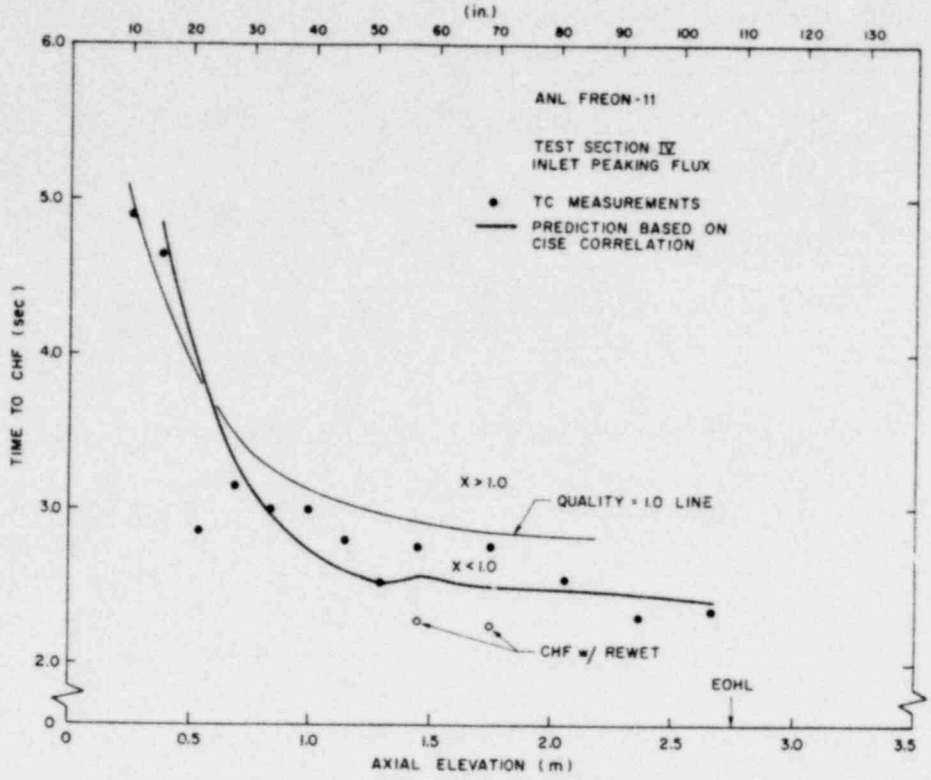

Fig. I.12. Prediction of CHF during Outlet Break Test DB-315. ANL Neg. No. 900-79-620.

In summary, the present analysis using a simple thermal-hydraulic code in combination with an appropriate CHF correlation can predict CHF onset during a wide range of flow transient. Future analyses will be extended to include a combination of flow and pressure transients, with and without flow reversals, and complex geometries.

References

1. C. L. Wheeler et al., COBRA-IV-I: An Interim Version of COBRA for Thermal Hydraulic Analysis of Rod Bundle Nuclear Fuel Elements and Cores, BNWL-1962 (1976).

2. J. E. Meyers, Hydrodynamic Models for the Treatment of Reactor Thermal Transients, Nucl. Sci. Eng. 10, 269 (1961).

3. W. T. Hancox and S. Banerjee, Numerical Standards for Flow-Boiling Analysis, Nucl. Sci. Eng. 64, 106 (1977).

4. W. T. Hancox, W. G. Mathers, and D. Kawa, "Analysis of Transient Flow-Boiling; Application of the Method of Characteristics," Paper 42, AIChE 15th Nat. Heat Transfer Conf., San Francisco, CA (1975).

5. G. B. Wallis, One-Dimensional Two-Phase Flow, McGraw-Hill (1969).

6. D. Moxon and P. A. Edwards, Dryout During Flow and Power Transients, AEEW-R-553 (1967).

7. R. Roumy, "Burnout in Transient Conditions in Circular Tubes," European Two-Phase Flow Group Meet., Harwell (1974).

8. M. Cumo et al., Transient Critical Heat Flux in Loss-of-Flow Accidents, RT/ING (77) 14 (1977).

9. D. Moxon, SLIP--A Dynamic Program for the Thermal-hydraulic Behavior of Boiling Loops, AEEW-R-448 (1968).

10. R. W. Bowring, A Simple but Accurate Round Tube, Uniform Heat Flux Dryout Correlation Over the Pressure Range 0.7-17 MN/m^2, AEEW-R789 (1972).

11. L. Biasi et al., Studies on Burnout: Part 3, Energ. Nucl. 14, 530 (1967).

12. S. Bertoletti et al., Heat Transfer Crisis with Steam-Water Mixtures, Energ. Nucl. 12, 121 (1965).

13. P. B. Whalley et al., "Calculation of the Variation of Dryout Length Under Transient Conditions in Two-Phase Flow," 5th Symp. on Computers in Chemical Engineering, Czechoslovakia Chemical Society, Czechoslovakia (1977).

14. P. B. Whalley et al., "The Calculation of Critical Heat Flux in Forced Convection Boiling," 5th Int. Heat Transfer Conference, Tokyo, Paper B6.11 (1974).

15. M. Cumo et al., "Prediction of Burnout Power with Freon Up to the Critical Pressure," European Two-Phase Group Meet., Casaccia, Rome (1972).

16. Light-water-reactor Safety Research Program: Quarterly Progress Report, October-December 1978, NUREG/CR-0828, ANL 79-13 (Apr 1979).

17. R. T. Lahey et al., "The Effect of Nonuniform Axial Heat Flux on Critical Power," Proc. Heat and Fluid Flow in Water Reactor Safety, p. 193 (1977).

II. TRANSIENT FUEL RESPONSE AND FISSION-PRODUCT RELEASE PROGRAM

Principal Investigators
J. Rest and S. M. Gehl, MSD

A. Introduction and Summary

A physically realistic description of fuel swelling and fission-gas release is needed to aid in predicting the behavior of fuel rods and fission gases under certain hypothetical light-water-reactor (LWR) accident conditions. To satisfy this need, a comprehensive computer-base model, the Steady-state and Transient Gas-release and Swelling Subroutine (GRASS-SST), is being developed at Argonne National Laboratory (ANL). This model is being incorporated into the Fuel-rod Analysis Program (FRAP) code being developed by EG&G Idaho, Inc., at the Idaho National Engineering Laboratory (INEL).

The analytical effort is supported by a data base and correlations developed from characterization of irradiated LWR fuel and from out-of-reactor transient heating tests of irradiated commercial and experimental LWR fuel under a range of thermal conditions.

Emphasis in the early stages of the program has been on thermal conditions in pressurized-water-reactor (PWR) fuel that are applicable to anticipated hypothetical power-cooling-mismatch (PCM) accidents. Recent efforts include conditions typical of other types of hypothetical accidents. The program is also developing information on fission-gas release during steady-state and load-following operations.

Recent significant experimental and analytical advances at the end of this quarter are summarized below:

1. GRASS-SST predictions for high-burnup gas release are in reasonable agreement with the data of Zimmermann.[1]

2. In-cell installation and checkout of the replacement DEH test chamber and specimen-preparation containment box have been completed. The experimental DEH-testing program is now ready to resume.

B. Modeling of Fuel/Fission-product Behavior (J. Rest, MSD)

1. High-burnup Fission-gas Release

a. Introduction

GRASS-SST analyses this quarter of high-burnup (~10 at. %) fission-gas release data of Zimmermann[1] for fuel temperatures between

1250 and 2000 K has demonstrated that the code is unable to predict the measured releases. Zimmermann's experiments were designed to provide relatively small thermal gradients across the fuel pellets. (Quantitative information on the size of the gradients is not available.) Sensitivity analyses with GRASS-SST indicate that a reasonable spread in the uncertainties in the values of the thermal gradients are unable to account for the differences between prediction and measurement. For example, GRASS-SST predicts <1% gas release for the 1250 K experiment, whereas, ~55% gas release was measured. In order to best gain a perspective on the nature of the deficiency in the code, which prevents the prediction of Zimmermann's high-burnup gas-release data, it is appropriate at this time to review some of the history and methodology of GRASS-SST code development.

b. Paths for Fission-gas Release

A current problem in the modeling of fission-gas behavior is identification of the dominant mechanisms of fission-gas mobility in nuclear fuels. Fission gas (xenon and krypton) is generated through nuclear fission, primarily within the UO_2 (or U-PO_2) grains. These gases are relatively insoluble within the UO_2 matrix and tend to nucleate into bubbles. The bubbles can grow by coalescence and gas-atom diffusion, and can shrink by re-solution. The fission gas can migrate both in atomic form and in bubbles by either random or biased (in a temperature gradient) motion to the grain boundaries, where the bubbles tend to grow. Grain-boundary bubbles may also be susceptible to the effects of re-solution. Subsequently, the fission gas on the grain boundaries can migrate to the grain edges.

In addition, if the grain boundaries become saturated with gas, channels can form through bubble coalescence, enabling the gas to rapidly vent to the grain edges. Gas reaching a grain edge deforms the edge and contributes to the degree of interconnection between grain edges. If the grain edges and corners are interconnected to a free surface, the gas can escape to the exterior of the fuel. Alternatively, grain boundaries weakened by the accumulation of fission gases (and other fission products) may fracture extensively under stress and enable the gas to vent directly to the fuel-cladding gap. Fission gas retained in the fuel contributes to fuel swelling.

The above scenario for gas migration from the interior to the exterior of the fuel is, in general, widely accepted and is the one upon which GRASS-SST is based.[2] However, an overall understanding of, and capability to predict, fission-gas behavior in nuclear fuels is hampered by a lack of detailed knowledge of the various processes involved in this migration. One is interested in predicting the response of fission gas during normal operation as a function of fuel properties (e.g., grain size and grain growth), fuel temperature and temperature gradient, power rating, and burnup; and during transient or off-normal operation, as a function of irradiation history (e.g., power rating and burnup) and accident scenario (e.g., heating-rate history). Consistency requires that, once a set of models has been developed to

describe the synergistic interplay of the multitude of processes involved in fission-gas behavior, they be applicable under the full range of normal and off-normal conditions of interest. However, given the current range of uncertainties in the properties and mechanisms of fuel and fission-gas response, the ability of any particular model of fission-gas behavior to predict results for a broad range of conditions is not obvious.

C. Bubble Diffusivities and Gas-atom Re-solution

For gas to be released from the fuel, it must first be expelled from its birthplace within the grains. The rate at which the gas is released to the grain boundaries during normal operation depends, in general, on the atomic and gas-bubble diffusivities and on the gas-atom re-solution rate. Under conditions in which bubble mobility is minimal (low-moderate temperature regime), the forward flux of intragranular gas to the boundaries is composed mainly of the atomic species; the relatively immobile gas bubbles act as gas-atom trapping sites. The average time that a gas atom spends trapped in a bubble before it is knocked back into solution, either direction or indirectly, by a fission fragment is given by the inverse of the re-solution rate, b. Fission-gas bubbles located on the grain boundaries also undergo re-solution, and this can create a backward flux of gas atoms into the lattice. Clearly, the rate of fission-gas release to the grain edges, and the overall dependence of this release rate on the value of b, is a strong function of the relative magnitudes of the forward and backward fluxes of gas atoms. For example, if the forward and backward fluxes are of the same magnitude, the rate at which fission gas arrives at the grain edges will be relatively insensitive to the irradiation time. In general, the rate at which fission gas arrives at the grain edges will be a strong function of b; this rate will increase or decrease with an increase in b, depending on whether the forward flux is, respectively, greater or less than the backward flux.

The magnitude of the backward flux is primarily a function of b (as is the forward flux), intergranular bubble size, and the probability that an atom ejected from a grain-boundary bubble actually reenters the lattice, that is, the probability that an atom travels a re-solution distance d_R that is large compared to the grain-boundary gas-atom recapture distance d_c. The latter is the maximum distance a gas atom can move from the boundary before losing a high-diffusivity path back to the grain surface. (The intergranular atomic and gas-bubble diffusivities are thought to be substantially higher than those for intragranular fission gas, owing to the existence of ledges on the grain surface.) For intergranular bubble sizes that are small compared to d_R, the magnitude of the backward flux depends essentially on b and on the relative magnitude between d_R and d_c. For bubble sizes that are large compared to d_R, the magnitude of the backward flux is relatively independent of b; on the average, "knocked" gas atoms do not travel far enough within the bubble to escape from it and thus remain trapped.

For the low-moderate temperature environments where the bubble mobility is low, the rate of gas release will be mainly re-solution controlled, and will be relatively insensitive to changes in the intragranular gas-atom and bubble diffusivities. However, because the ratio between the forward and backward gas-atom fluxes is dependent on intra- and intergranular bubble sizes, and since these bubble sizes are, in general, dependent on the irradiation time, fuel temperature, and rating, the overall dependence of the fission-gas release rate on b will, in general, be a function of the fuel power history and burnup.

Within high-temperature and high-temperature-gradient environments (e.g., the columnar-grain-growth region), where the gas bubbles have substantial mobility, the rate at which the gas reaches the grain edges will be relatively insensitive to b and strongly dependent on the value of the gas-bubble diffusivity. On the other hand, the average size of such bubbles will be dependent on b, and thus the velocity of these bubbles, which is in general a function of their size, will be indirectly dependent on b. However, within the high-temperature environment, the bubbles are expected to grow to sizes much larger than the re-solution distance, and thus the dependence of bubble velocity on re-solution rate will be minimal.

The above discussion indicates that an accurate (i.e., GRASS-SST) description of intra- and intergranular fission-gas behavior requires quantitative information on the gas-atom and bubble diffusivities, re-solution rate, re-solution distance, grain-boundary gas-atom recapture distance, and physically realistic descriptions of the interactive dependence of fission-gas behavior on these parameters.

D. Gas-bubble Swelling, Grain-edge Porosity Interconnection, and Grain-boundary Separation

Once the fission gas has reached the grain edges, it remains trapped there unless a path exists from the grain edges to the exterior of the fuel. Experimentally, it has been observed[3] that long-range interconnection of grain-edge porosity is a function of the strain due to grain-edge gas-bubble swelling. Thus, to calculate the rate of fission-gas release from the fuel, one must be able to calculate the evolution of, first, the grain-edge gas-bubble swelling, and second, the grain-edge porosity interconnection. These calculations are further complicated by the apparent influence[4] of the as-fabricated porosity on the degree of grain-edge porosity interconnection (at least for fuel densities less than approximately 90% TD).

The accumulation of fission gas (and other fission products) on grain boundaries and edges tends to degrade the strength of the boundary, and grain-boundary separation may result if the stresses on the boundary exceed the boundary fracture strength. Experimentally, a change in the mode of fuel fracture from predominantly intra- to intergranular has been observed[5] in

high-burnup fuel irradiated at relatively low temperatures. Extensive grain-boundary separation has been observed[6] to occur during the DEH transient heating tests on irradiated commercial UO_2 fuel. A correlation has been noted between the increase in pore-solid interfacial surface area during these tests and the amount of fission gas released. SEM examination of the tested specimens indicates that intergranular separations can form by the diffusion-controlled processes of growth and coalescence of fission-gas bubbles.

In addition, this gradual process of bubble growth and coalescence to form channels and channel coalescence to form separations can be interrupted by the more rapid process of crack propagation. Crack propagation results from stresses on weakened grain boundaries. The stresses responsible for cracking are the result of applied axial load, differential thermal expansion, solid fission-product swelling, and the pressurization of intergranular fission-gas bubbles. Grain-boundary separation has also been observed[7] in fuel tested in the PBF reactor in Idaho and in commercial fuel that had undergone a power excursion in the Dresden reactor in Illinois.

Thus, to accurately predict the release of fission gas from grain boundaries and edges, one must be able to calculate not only the evolution of the grain-edge porosity interconnection, but also the onset and degree of grain-boundary separation. These two phenomena are somewhat interdependent in that they are both precipitated, in part, by the accumulation of fission gas. Whether one or the other or both phenomena occur is dependent on fuel type (e.g., grain size or density) as well as on the particular operating scenario consideration.

E. Fission-gas Bubble Mobilities during Transient Heating and the Prediction of Fission-gas Behavior under Normal Irradiation Conditions

Several researchers,[8,9] including the present author,[2] have been forced to the conclusion that bubble mobility during transient heating is greater than during normal irradiation conditions. However, the present author concurs with those who think it is rather risky to make model predictions, especially for time scales where little experimental data are available, without having clarified the basic mechanisms of gas-bubble behavior under normal irradiation conditions.

Model predictions for fission-gas behavior during normal irradiation conditions can be compared with many types of measurements, when available: intra- and intergranular bubble-size distributions, gas release, radial distribution of retained gas, amount of fission gas at grain boundaries and edges, fuel swelling, and so on. These measurements (and predictions) can be made for fuels of various types irradiated at different temperatures, power ratings, and burnups. Comparing predictions with only a small subset of data (for example, only total gas-release measurements) is unsatisfactory in that information on the particular fission-gas behavioral mechanisms operative is

not readily apparent and thus is not readily verifiable. Identification of fission-gas behavioral mechanisms is essential for a thorough understanding of the phenomena, and for assuring the applicability of the models to other operating environments. Unfortunately, verification of model predictions is hindered by the inadequacy of the available data.

To develop and verify models describing a broad range of phenomena, one requires specific data spanning the conditions of interest. Unfortunately, this type of data is not generally available. For example, data from high-burnup irradiations consist mainly of fission-gas release measurements. Still lacking are data on the size and morphology of the fission-gas bubbles, fuel microstructure, etc. In addition, most high-burnup data are from fuel pins of varying types and power ratings. Thus it is a complex, if not impossible, job to sort out the specific mechanisms that resulted in the release of the gas (for example, temperature-dependent versus burnup-dependent phenomena).

Heretofore, GRASS-SST development and verification was primarily based on certain specific data which were available at the time; i.e., intragranular bubble sizes in, and total fission-gas release from, as-irradiated relatively low-burnup; low-temperature (H. B. Robinson) fuel; gas release from as-irradiated relatively low-burnup, high-temperature (Saxton, CVTR) fuel; and the results of DEH transient tests on the fuel irradiated in the Saxton and H. B. Robinson reactors. Values for the bubble diffusivity, re-solution rate, and re-solution distance were chosen such that they were compatible with the uncertainties in the measured values, and the model predictions for as-irradiated intragranular bubble size agreed with the data. In addition, a value for the fraction of intergranular gas undergoing re-solution that re-enters the lattice was chosen such that when coupled to the models for grain-boundary-bubble diffusion and grain-edge porosity interconnection, the calculations for total gas release were also in agreement with the data. Thus, relative values for the intragranular bubble diffusivity and gas-atom re-solution rate, and a value for the fraction of intergranular gas undergoing re-solution which reenters the lattice, were chosen such that when combined with the models for the evolution of the grain-edge porosity accounted for the experimental measurements on the as-irradiated fuel.

Note that the GRASS-SST (empirically-based) values for intragranular bubble diffusion are significantly smaller than those predicted by the theoretical treatment of bubble mobility by surface diffusion. The physical basis for this apparent discrepancy is as follows. Under equilibrium conditions, the bubbles may be faceted, and the rate of motion of a faceted bubble is determined by the frequency of nucleation of steps instead of the time required for atoms to move from a step on one side of a bubble to a step on the other side. That is, the atom attachment and detachment rate is slower than predicted by surface diffusion. The GRASS-SST values for grain-boundary bubble diffusivities are close to the values predicted by the theoretical treatment of bubble mobility by surface diffusion. This choice is reasonable because of the ledging along the boundary surface, which should facilitate enhanced diffusion.

Subsequently, these calculations were used to predict the release of gas during DEH transient-heating tests on irradiated H. B. Robinson fuel pellets. The results showed that the predictions were significantly lower than the measured gas-release results and significantly higher than the measured intragranular bubble sizes. After exhausting all other possibilities, we reached the conclusion that all the evidence pointed toward enhanced mobilities during transient (nonequilibrium) conditions. A description of the noninstantaneous rate of growth of coalescing bubbles was initially included, on the supposition that the absence of this model caused the earlier discrepancies. However, further analyses indicated that, although the inclusion of this model resulted in acceptable calculated posttransient intragranular bubble sizes, the prediction of transient fission-gas release was still substantially below the measured values (i.e., the reduction in calculated size of the intragranular bubbles did not increase their mobility enough to account for the observed releases). Thus, one was led to the hypothesis that during transient heating the mobilities are increased beyond their as-irradiated values.

Bubbles intersected by dislocations have higher diffusivities than bubbles in a perfect lattice.[10] The bubble diffusivities were satisfactorily described by a rate-controlling nucleation mechanism, in which ledges introduced into the bubble surface by the dislocation rotated about the dislocation, causing the bubble to migrate. Since dislocations may extend to the grain surfaces, they can serve as channels that facilitate the migration of the bubbles out of the grains to the grain boundaries. During steady-state heating, the dislocation density is relatively small, and the effective diffusivities of the intragranular bubbles would not be expected to be appreciably altered.

However, during transient heating, differential thermal expansion and external loads can increase dislocation densities. The stress field around an overpressurized bubble can lead to additional increases in the dislocation density near the bubble. Overpressurization is due to a lack of vacancies in a lattice that is not in thermodynamic equilibrium. If the overpressure in a bubble results in an equivalent stress that exceeds the yield strength of the UO_2, then plastic deformation of the material around the bubble will result. Since the bubble surface intersects the resultant dislocations, ledges are produced that can facilitate atom attachment and detachment.

Since plastic deformation of the UO_2 due to an overpressurized bubble is expected to result in a high density of dislocations around the bubble surface, the diffusivity of such a bubble would be expected to increase rapidly. In effect, bubble diffusion would depend more on the time required for atoms to move from a step on one side of a bubble to a step on the other (i.e., surface diffusion) than on the frequency of nucleation of steps.

As the lattice approaches thermodynamic equilibrium, the bubbles expand at a faster rate, as a result of the availability of lattice vacancies, and lose their overpressurization. When the material around a bubble is no longer

undergoing plastic deformation, the dislocations quickly anneal out. Under these conditions, bubble mobility is quickly reduced as the diffusion of the bubbles becomes once again dominated by the frequency of step nucleation.

Subsequently, the above model for the enhanced mobilities of fission-gas bubbles during nonequilibrium heating conditions was included in the GRASS-SST calculations; this resulted in satisfactory predictions of fission-gas release during the transient. We had thus arrived at a "state-of-the-art" statement about the behavior of fission gas during normal and off-normal operating conditions consistent with the available data.

F. High-burnup Fission-gas-release Predictions

However, as stated in the introduction, analyses performed this quarter have shown that GRASS-SST is unable to account for the substantial releases of fission gas from low-temperature, high-burnup fuel pellets; the calculations result in predictions of fractional fission-gas release that are significantly smaller than what is actually observed.

Subsequent analyses have resulted in the following observations. At low temperature, the calculations predict a backward flux of gas atoms into the lattice due to grain-boundary-bubble re-solution of the same magnitude as the forward flux of gas from the lattice to the grain boundaries. Thus, very little gas is available for transport to the grain edges. This situation is relatively insensitive to the degree of burnup. Several possible remedies come to mind. The intragranular diffusivities could be increased (at the same time, the re-solution rate should be increased in order to retain the prediction of intragranular bubble size), or the effectiveness of grain-boundary-bubble re-solution could be decreased, or both. The prediction of gas release for the as-irradiated condition would be relatively unaffected by a decrease in the effectiveness of intergranular re-solution because the irradiations were at a relatively high temperature where bubble mobility would be substantial and/or at a relatively low burnup. Thus, this choice would perhaps be the most reasonable and, in fact, is the one that has been implemented into the GRASS-SST code.

In principle, intragranular bubble diffusivities under irradiation conditions could approach those predicted by the theory of surface diffusion. The effect of facets on the bubble surface, which appear to be the reason for the reduced mobilities observed during isothermal anneals, might be obscured a great degree during irradiation as a result of irradiation damage and associated vacancy and defect production. In turn, higher values of the re-solution rate might be more in line with current experimental results.

The grain-boundary-bubble re-solution rate could be reduced by either growing larger grain-boundary bubbles such that the bubble size is much larger, on the average, than the re-solution distance, or by using a re-solution

distance smaller than the grain-boundary gas-atom recapture distance. The ejected gas atoms then travel high-diffusivity paths back to the gas bubble so that, effectively, they have not been lost from the bubble. More definite answers to the questions raised in the above discussion must await further experiments and analyses of the observed phenomena.

Figure II.1 shows GRASS-SST predictions for fission-gas release as a function of burnup for irradiations at 1250, 1500, 1750, and 2000 K, respectively, compared with the data of Zimmermann.[1] As discussed above, the calculations shown in Fig. II.1 were made after implementing into the code the assumption that grain-boundary-bubble re-solution is considerably less effective than intragranular-bubble re-solution; the value for the grain-boundary-bubble re-solution rate used in GRASS-SST is three orders of magnitude less than that used for intragranular bubbles. As shown in Fig. II.1, the GRASS-SST predictions of gas release at low and at high burnups are in reasonable agreement with the data.

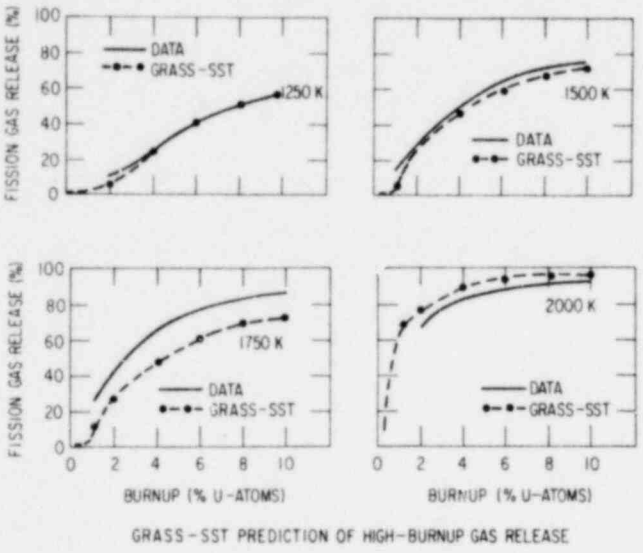

Fig. II.1. GRASS-SST Prediction of High-burnup Gas Release

Although the reduction in the strength of the grain-boundary-bubble re-solution rate had a minimal effect of the predicted gas release from the H. B. Robinson fuel, the predicted values for the amount of retained gas on grain-boundaries and edges and the grain-boundary-bubble sizes were somewhat increased from their previous values. Thus, since the predicted initial conditions in the fuel have changed, the predicted behavior during the DEH transient heating tests is expected to be somewhat modified. Analyses along these lines are continuing and will be described in upcoming quarterly reports.

G. Experimental Program (S. M. Gehl, MSD)

1. Replacement DEH Chamber (S. M. Gehl, D. S. Butler, and D. R. Pepalis, MSD)

All the effort in the experimental program was directed toward in-cell installation and checkout of the replacement DEH chamber and specimen-preparation containment box. A few minor problems with the electrical connections to the test chamber were discovered; these were easily corrected. More serious difficulties were encountered with the containment box. For example, the box was found to have several leaks, the location of

which was hampered by problems with the leak-detection equipment. The difficulty of correcting the problems associated with the test chamber and containment box was compounded by the necessity of making all repairs while the equipment was inside the hot cell.

All these problems resulted in a two-month delay in the DEH test program. However, by the end of the reporting period, the equipment was in working order and DEH testing was scheduled to resume.

References

1. H. Zimmermann, "Investigation of Swelling in Mixed Oxides," Proc. Workshop on Fission Gas Behavior in Nuclear Fuels, EUR 6600 En, Karlsruhe, Germany (Oct 26-27, 1978).
2. J. Rest, GRASS-SST: A Comprehensive, Mechanistic Model for the Prediction of Fission-gas Behavior in UO_2-base Fuels during Steady-state and Transient Conditions, ANL-78-53 (June 1978).
3. J. A. Turnbull and M. O. Tucker, Swelling in UO_2 Under Conditions of Gas Release, Phil. Mag. 30, 47 (1972).
4. C. Ronchi, "Definition and Evaluation of the Pore-interlinkage Parameter," Light-water-reactor Safety Research Program: Quarterly Progress Report, July-September 1975, ANL-75-72, pp. 94-96 (Feb 25, 1976).
5. R. G. Bellamy and J. B. Rich, Grain-Boundary Gas Release and Swelling in High Burnup Uranium Dioxide, J. Nucl. Mater. 33, 64-76 (1969).
6. S. M. Gehl, M. G. Seitz, and J. Rest, Fission-gas Release from Irradiated PWR Fuel during Simulated PCM-type Accidents: Progress Report, NUREG/CR-0088, ANL-77-80 (May 1978).
7. S. M. Gehl, Comparison of Fission-gas Release and Mechanical Behavior during Transient Nuclear and Electrical Heating of Light-water-reactor Fuels, ANL-78-60 (June 1979).
8. M. H. Wood and M. R. Hayns, "A Current View of the Theory of Fission Gas Precipitation Into Intra- and Intergranular Porosity," Proc. Workshop on Fission Gas Behavior in Nuclear Fuels, EUR 6600 En, Karlsruhe, Germany (Oct 26-27, 1978).
9. J. R. Matthews and M. H. Wood, "The Role of Fission Gas Swelling and Release in Fast Reactor Accidents," Ibid.
10. W. G. Beere, The Nucleation of Atomic Steps on Inert Gas Bubbles Intersected by Dislocations, Phil. Mag. 25, 189-200 (1972).

III. MECHANICAL PROPERTIES OF ZIRCALOY

H. M. Chung and T. F. Kassner, MSD

A. Summary

Since diametral-compression data on oxidized Zircaloy cladding were considered in the establishment of the present oxidation limits in the acceptance criteria for emergency-core-cooling systems (ECCS's) in light-water reactors (LWR's), the compression properties of ballooned and ruptured tubes were evaluated for comparison with results from ring-compression tests on segments of undeformed[1] and deformed[2,3] cladding after oxidation in steam. Information on the plastic deflection to maximum load, the total deflection to pellet-cladding contact or fragmentation, and the integrated energies to maximum load and fragmentation was obtained from load-deflection curves at 300 K. The results were correlated with various measured and calculated oxidation-related parameters and the hydrogen content of the cladding.

Although the tube-compression data were not sufficient to define a failure boundary for cladding-pellet contact relative to the time-temperature oxidation conditions, the results conclusively show that the 0.3-J impact-failure boundary provides a more severe limitation on the oxidation conditions.

Several tensile tests were performed to determine the strength and ductility of ballooned and ruptured cladding after long-term oxidation in steam. The results indicate that the cladding can sustain quite large loads (100-500 kg); however, the total elongations are small (≤3 mm for a 200-mm-long specimen).

Based upon the thermal-shock, impact, and diametral-compression properties of oxidized Zircaloy cladding and quantitative correlations of this information with various oxidation-related parameters, embrittlement criteria that encompass the mechanical response of the cladding under different loading modes have been formulated. Oxidation limits to ensure that the cladding can withstand thermal-shock and mechanical loads during LOCA situations in LWR's were stated relative to the minimum cladding wall thickness with a specified maximum oxygen concentration. The criteria are applicable irrespective of the oxidation temperature, initial wall thickness, wall thickness that results from deformation under internal pressure, and the total oxygen content of the cladding.

B. Diametral Tube-compression Properties of Ruptured Zircaloy-4 Cladding

The deformed cladding that survived thermal shock and impact loads, corresponding to energies of 0.15 and 0.3 J, was used to evaluate the diametral-compression properties at 300 K. Figure III.1 is a schematic representation of a ruptured tube and the sequence of axial locations in which the compression

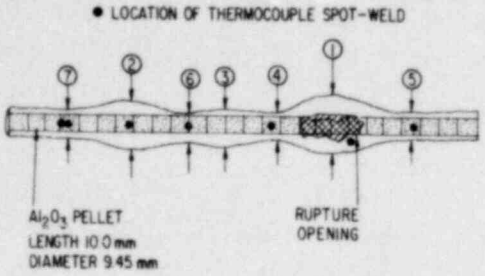

Fig. III.1. Schematic Representation of a Zircaloy Cladding Specimen after Rupture in Steam Showing the Sequence of Axial Locations for Compression Tests Used to Determine the Deflection to Produce Fragmentation or Pellet-Cladding Contact. ANL Neg. No. 306-79-400.

tests were performed. The diameter of the cladding in each location was measured before the test in the directions parallel and perpendicular to the axis of compression. The region of largest diameter, usually near the rupture location, was compressed first, followed by other ballooned regions, and lastly the regions of small diametral expansion adjacent to the ballooned regions for which the time-temperature history was known. Compression of each location at a rate of 0.04 mm/s was continued up to the moment of cladding fragmentation or cladding-pellet contact. The time at which the cladding contacted the alumina pellet could easily be detected as indicated by the abrupt increase in load in Fig. III.2. When the cladding fragmented before cladding-pellet contact, the load dropped abruptly to a small value as shown on the load-deflection curve in Fig. III.3.

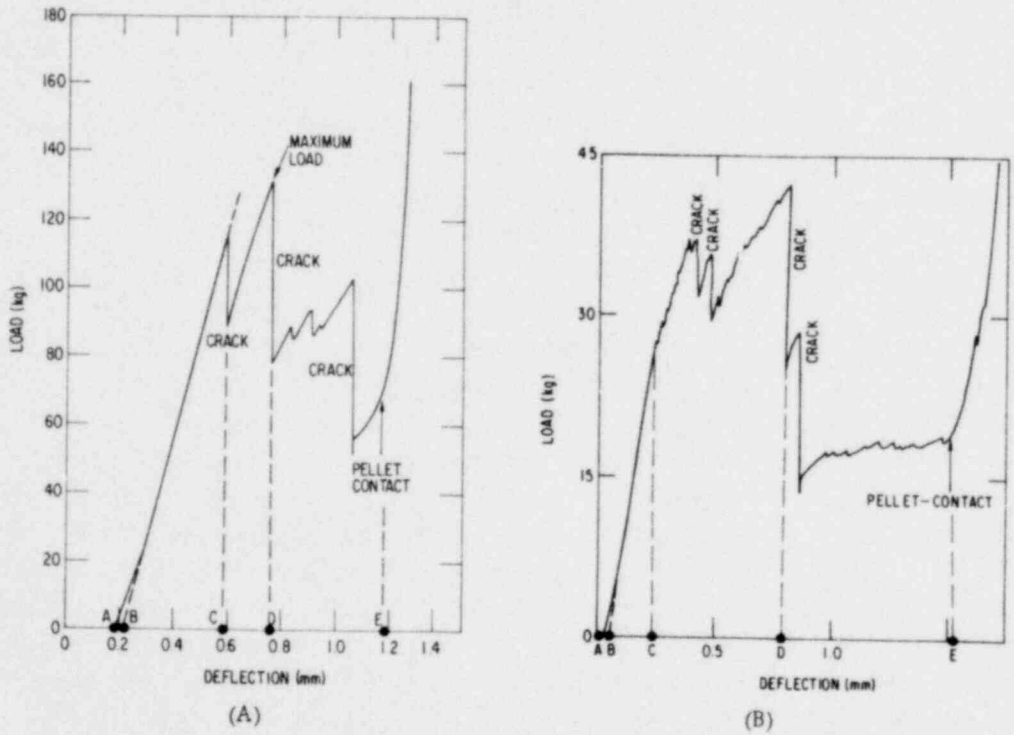

Fig. III.2. Typical Load-vs-Deflection Curves from Diametral Tube-compression Tests on Ruptured Zircaloy-4 Cladding Showing an Abrupt Increase in Load due to Contact between the Cladding and Pellet. The tube was ruptured at ~1055 K, oxidized in steam for 1840 s at a maximum temperature of 1419 K, cooled to ~1100 K at ~5 K/s, and flooded with water. The specimen survived thermal-shock and pendulum impact at an energy of 0.3 J at 300 K. The load-deflection curves correspond to the following conditions: (A) ~80 mm from the rupture center, circumferential strain ~0.06, temperature 1287 K, and (B) ~35 mm from the rupture center, circumferential strain 0.122, temperature 1353 K. ANL Neg. Nos. 306-79-416 and 306-79-395 Rev. 1.

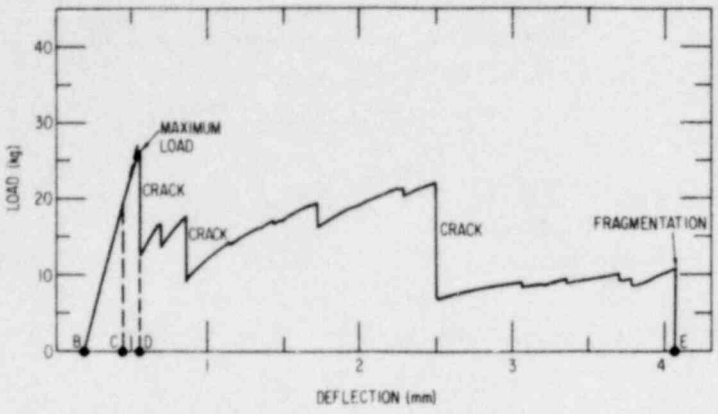

Fig. III.3

Typical Load-vs-Deflection Curve from Diametral Tube-compression Test on Ruptured Zircaloy-4 Cladding Showing an Abrupt Decrease in Load due to Fragmentation of the Tube. The load-deflection curve corresponds to the following conditions: compression at the rupture center, circumferential strain 0.74, oxidation time and temperature 1840 s and 1303 K, respectively. ANL Neg. No. 306-79-408.

Segments of the cladding were retained after the compression tests for metallographic evaluation and hydrogen analyses. The thicknesses of the oxide, stabilized-α, and transformed β-phase layers were determined by either optical or scanning-electron microscopy. If the local temperature during the isothermal oxidation period was not constant within ±7 K, metallographic and hydrogen analyses were not performed on the material. The hydrogen analyses and the measured and calculated oxidation parameters are tabulated in Sec. III.D below, along with the mechanical-deformation data.

To enable a relative comparison of the capability of the oxidized cladding to survive deformation by impact[1] and compressive loads at room temperature, the tube-compression data (i.e., the time-temperature conditions for which the cladding encountered pellet contact, or a total deflection of >3 mm and a total integrated energy to fragmentation of >0.3 J in a slow compression test) are plotted in Fig. III.4. The open symbols denote cladding

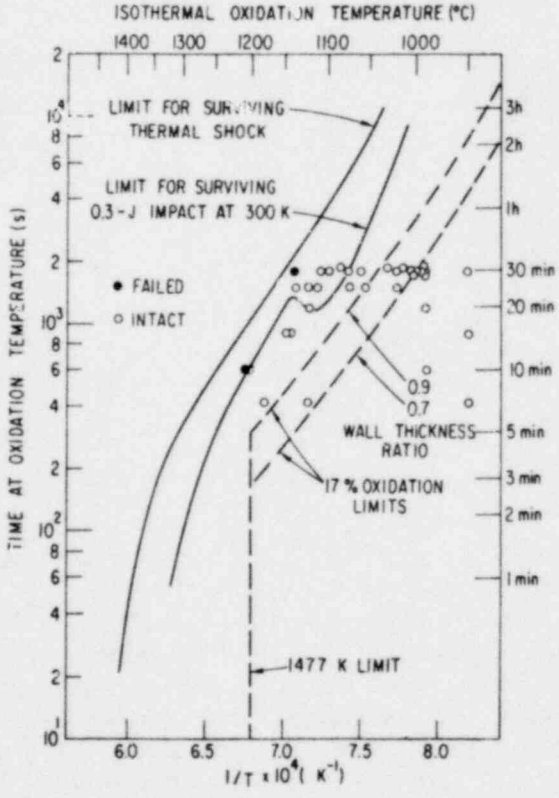

Fig. III.4

Time-Temperature Oxidation Conditions for Ruptured Zircaloy-4 Cladding Which Survived Slow Diametral Compression (0.04 mm/s) to the Point of Cladding/Pellet Contact, or Total Deflection of >3.0 mm and a Total Integrated Energy to Fragmentation of >0.3 J. Shown for comparison are "best-estimate" time-temperature failure boundaries for thermal shock and 0.3-J room-temperature impact as well as the 17% ECR oxidation limits for cladding with two wall-thickness ratios. Calculated ECR limits are based on oxidation of the inner and outer surfaces of the cladding. ANL Neg. No. 306-79-412 Rev. 1.

that met these conditions (i.e., "intact") in contrast to tubes that fragmented before either a total deflection of <3 mm or a total integrated energy of <0.3 J was attained (i.e., "failed"). For comparison, Fig. III.4 also shows the best-estimate 0.3-J impact- and thermal-shock-failure boundaries as well as the calculated 17% equivalent-cladding-reacted (ECR) oxidation limits for cladding with two wall-thickness ratios.

Although the tube-compression data are not sufficient to satisfactorily define a failure boundary for cladding-pellet contact, the time-temperature oxidation conditions in Fig. III.4 show conclusively that the 0.3-J impact-failure boundary provides a more severe limitation on the oxidation conditions; i.e. cladding that survives an impact energy of 0.3 J will necessarily withstand thermal-shock loads, diametral deflections of ~3 mm without fragmentation, and an integrated energy from the load-deflection curve of ~0.3 J.

In contrast to the properties at fracture, values for the deflection and integrated energy to the point of maximum load on load-deflection curves from the tube-compression tests provide a better basis for comparison with results from compression tests on ring segments of undeformed cladding[1] and data from ring segments of deformed cladding obtained by Kawasaki et al.[2,3]

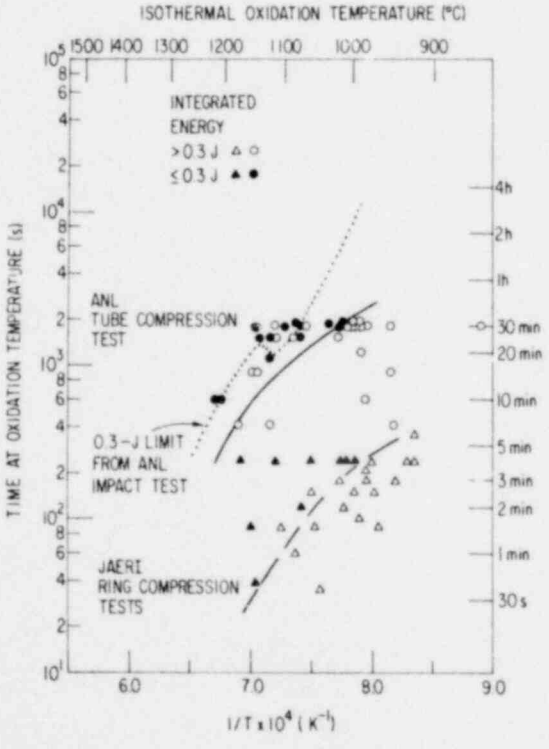

Fig. III.5

Time-Temperature Oxidation Conditions Resulting in Integrated Energies to Maximum Load above and below 0.3 J from Load-vs-Deflection Curves during Slow Diametral Compression of Tube (this study) and Ring Specimens[2,3] at 300 and 373 K, Respectively. The 0.3-J impact-failure boundary from tests on identical tubes is shown for comparison. ANL Neg. No. 306-79-398.

In Fig. III.5, the time-temperature conditions during oxidation that result in an integrated energy of ~0.3 J (calculated to the point of maximum load on a load-versus-deflection curve) were, in general, greater for the tube specimens in this investigation relative to the 15-mm-long ring specimens in the work of Kawasaki et al.[2,3] This occurs because the extent of oxidation and the hydrogen uptake characteristics of the ballooned and ruptured cladding in our experiments vary with axial position due to a nonuniform axial temperature profile. Consequently, an axial crack can propagate into regions of relatively tough material (i.e., less oxidation due to a lower temperature) and thus sustain a high load. Whereas the time-temperature conditions associated with impact and tube-compression failure boundaries of 0.3 J are similar, the 0.3-J failure boundaries deduced from ring-compression tests on deformed[2,3] as well as undeformed[1] cladding are considerably lower.

Figures III.6 and III.7 show the plastic deflection to maximum load as functions of the β-phase centerline oxygen

content and the hydrogen content of the cladding, respectively. These data are similar to the results obtained by Kawasaki et al.[2,3] from 15-mm-long ring segments of ballooned cladding, since the maximum load in a tube- or ring-compression test corresponds to the formation of the initial axial crack. Although the results in Figs. III.6 and III.7 indicate that the ductility decreases markedly as the oxygen and hydrogen concentration increase, the combined effect of these elements is better represented by the three-dimensional plot in Fig. III.8. For comparison, the figure includes several points calculated from the results of Kawasaki et al.[2,3] The effect of oxygen and hydrogen on the plastic deflection to the point of maximum load can be more easily visualized in Fig. III 9, obtained by interpolation of the data in the previous figure. The amount of plastic deflection to the point of the initial crack (i.e., maximum load) during slow diametral compression decreases rapidly as the oxygen and hydrogen concentrations in the cladding increase individually or in combination.

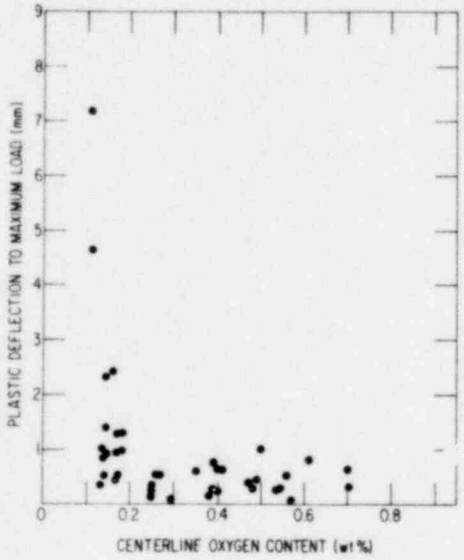

Fig. III.6

Plastic Deflection to Maximum Load at 300 K from Diametral Tube-compression Tests on Zircaloy-4 Cladding as a Function of β-phase Centerline Oxygen Concentration. ANL Neg. No. 306-79-414 Rev. 1.

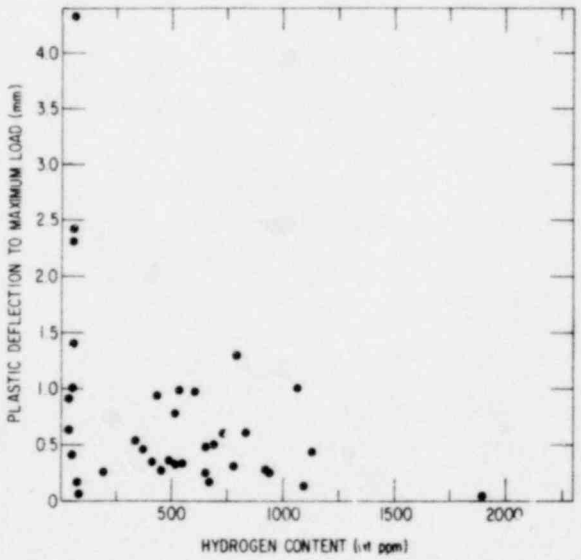

Fig. III.7

Plastic Deformation to Maximum Load at 300 K from Diametral Tube-compression Tests as a Function of Hydrogen Content of Zircaloy-4 Cladding. ANL Neg. No. 306-79-409.

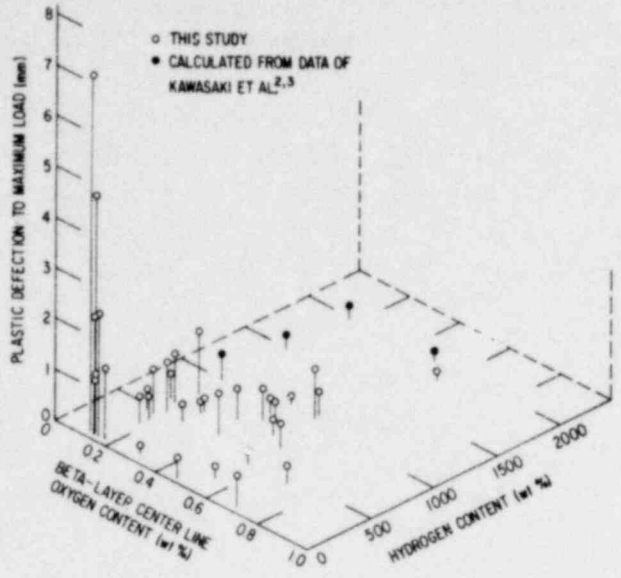

Fig. III.8

Three-dimensional Plot of Plastic Deflection to Maximum Load at 300 K from Diametral Tube-compression Tests as a Function of β-layer Centerline Oxygen Concentration and Hydrogen Content of Zircaloy-4 Cladding. ANL Neg. No. 306-79-837.

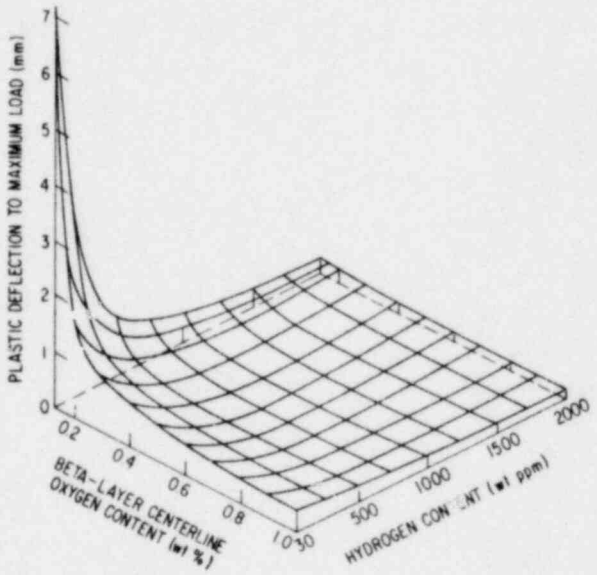

Fig. III.9

Three-dimensional Representation of Plastic Deflection to Maximum Load at 300 K Relative to β-layer Centerline Oxygen Concentration and Hydrogen Content of Zircaloy-4 Cladding Obtained from Interpolation of the Data in Fig. III.8. ANL Neg. No. 306-79-849.

In contrast to the thermal-shock-failure limit, the various measured and calculated properties from diametral-compression load-deflection curves do not provide an a-priori failure criterion that is applicable to Zircaloy fuel cladding under accident situations in LWR's, but are merely indications of material toughness determined by different methods.

C. Tensile Properties of Zircaloy-4 Cladding after Rupture and Oxidation in Steam

Several tests were performed to determine the tensile strength and ductility of ballooned and ruptured cladding after long-term oxidation in steam. The tests were performed to obtain semiquantitative information on the maximum tensile strength of cladding that had been oxidized in steam under time-temperature conditions near the 0.3-J impact-failure boundary.[1]

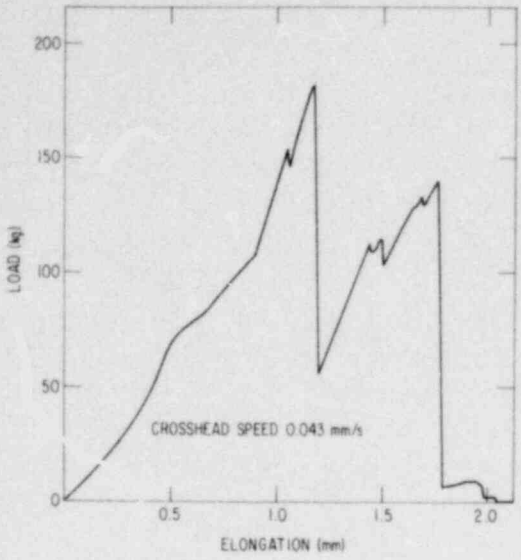

Fig. III.10

Load-vs-Elongation Curve at 300 K for a Zircaloy-4 Specimen Oxidized in Steam at 1218-1273 K for 30 min. Cooled to ~1100 K at 5 K/s, and Flooded with Water. Crosshead speed, 0.043 mm/s. ANL Neg. No. 306-79-987.

Figure III 10 is a typical load-elongation curve at 300 K for cladding that was ruptured and oxidized in steam, cooled through the temperature range of the $\beta \rightarrow \alpha'$ phase transformation at a rate of ~5 K/s, and bottom-flooded with water. Figure III.11 shows that the tensile fractures, which occur in the ballooned region, as well as at locations away from the rupture, are predominantly circumferential. The oxidation time and axial temperature variation for the specimens shown in Fig. III.11 are indicated by the horizontal bars in Fig. III.12. The relevant measured and calculated oxidation-related parameters, hydrogen content of the cladding, and load-elongation data are summarized in Sec. D below. Although the total elongations are small (≤3 mm), the loads are quite large (100-500 kg) for cladding that was oxidized on the inner and outer surfaces at maximum temperatures between ~1370 and 1420 K for periods ≥25 min.

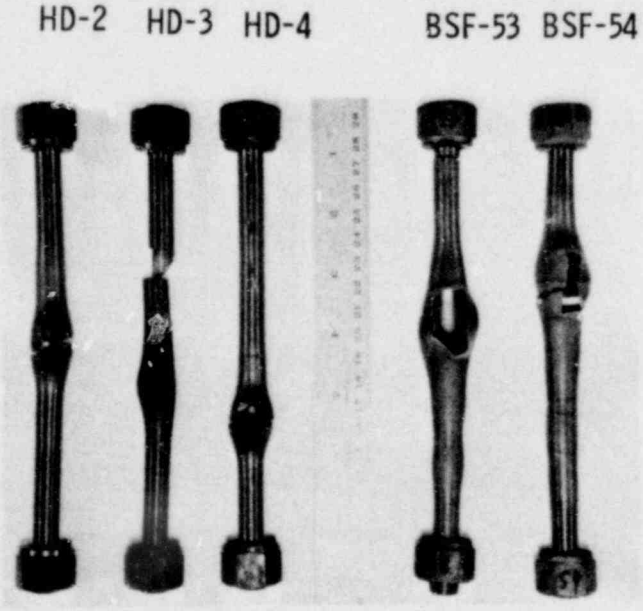

Fig. III.11

Zircaloy-4 Specimens after Oxidation in Steam and Tensile Testing at 300 K. A predominantly circumferential fracture occurs in contrast to fragmentation under an impact load. ANL Neg. No. 306-79-834.

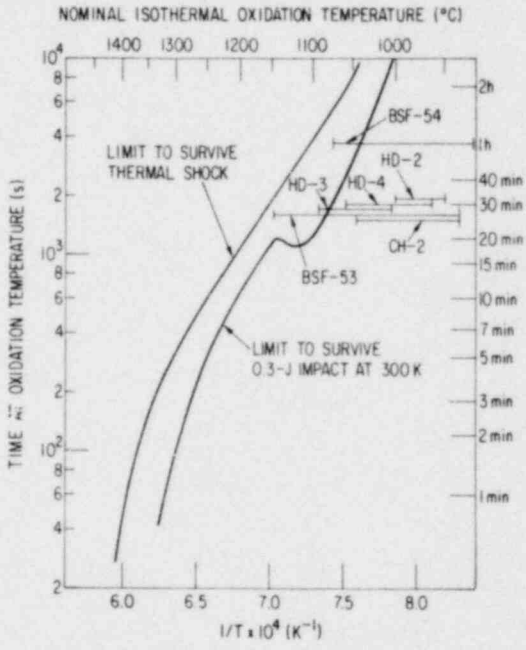

Fig. III.12

Time-Temperature Oxidation Conditions for Zircaloy-4 Specimens from Integral Tube-burst/Tensile Tests Shown in Fig. III.11. The horizontal bars indicate the axial temperature variation for each specimen. ANL Neg. No. 306-79-848.

D. Tabulation of Impact, Diametral Tube-compression, and Tensile Data for Ruptured Zircaloy-4 Cladding

Results from room-temperature impact, diametral tube-compression, and uniaxial-tensile tests on ruptured Zircaloy cladding after oxidation of the inner and outer surfaces in steam are tabulated in Tables III.1-III.3. Table III.1 contains data on the pendulum-impact properties of cladding, which was ruptured and oxidized in steam, cooled through the temperature range of the $\beta \rightarrow \alpha'$ phase transformation at a rate of ~5 K/s, and quenched by bottom-flooding with water. These data were presented graphically in previous reports. Table III.2 summarizes results from diametral tube-compression tests on cladding that survived both thermal-shock and impact loads, and Table III.3 contains data from six uniaxial-tensile tests on ruptured and oxidized cladding. The oxidation conditions, phase-layer thicknesses, oxidation-related parameters, and hydrogen content are specified along with the deformation properties.

E. Recommended Zircaloy Embrittlement Criteria Based upon the Results of This Investigation

Embrittlement criteria, which encompass the mechanical response of the cladding under different loading modes, have been formulated relative to the thermal-shock and impact resistance of material with critical thicknesses of the transformed β-phase layer containing maximum oxygen contents. Recommended embrittlement criteria based upon results from this investigation[4] are as follows:

1. Capability to Withstand Thermal Shock during LOCA Reflood

   The calculated thickness of the cladding with ≤0.9 wt % oxygen, based on the average wall thickness at any axial location, shall be greater than 0.1 mm.

2. Capability for Fuel Handling, Transport, and Interim Storage of Oxidized Fuel Assemblies

   The calculated thickness of the cladding with ≤0.7 wt % oxygen, based on the average wall thickness at any axial location, shall be greater than 0.3 mm.

The above criteria are applicable irrespective of the oxidation temperature, initial wall thickness, wall thickness that results from ballooning deformation, and the total oxygen content of the cladding. Since local hydrogen uptake by the cladding depends on a number of factors in addition to the time and temperature of oxidation, it is not possible to specify an upper limit that can be based upon readily controlled independent variables. For a wide range of experimental conditions of the integral tube-burst/thermal-shock tests, the influence of hydrogen at concentrations up to ~2200 ppm is incorporated in the thermal-shock and low-temperature deformation properties upon which the criteria are based.

TABLE III.1. Impact-test Results[a] on Deformed and Ruptured Zircaloy-4 Cladding That Survived Thermal Shock[b]

Test No.	ϵ_θ^{MAX}	BOA, mm^2	Temp., K	t, s	Z_{BF}, mm	D_1, mm	D_2, mm	WTR	I_S, J	I_F, J	FMC	C_H, wt. ppm	ζ_{ox}^{o}, 10^{-2} mm	ζ_{α}^{o}, 10^{-2} mm	ζ_{β}, 10^{-2} mm	ζ_{α}^{I}, 10^{-2} mm	ζ_{ox}^{I}, 10^{-2} mm	ECR, %	F_W	C_S^{CEN}, wt %	FBS, %	$L_{0.7}$, mm
PCD-11	0.79	101.4	1273	1800	94	11.7	11.5	0.97	0.3	-	33	335	5.5	5.5	50.8	1.3	0.2	8.14	0.83	0.17	94.78	0.508
-12	|	|	1278	|	65	11.8	11.7	0.97	|	-	|	795	5.2	4.4	48.9	1.2	5.7	13.06	0.80	0.17	95.66	0.489
-13	|	|	1270	|	35	12.5	12.4	0.85	|	-	|	535	5.0	4.8	38.6	4.4	5.0	14.40	0.71	0.18	97.94	0.386
-14	↓	↓	1260	↓	11	-	-	0.80	↓	-	↓	60	3.0	3.8	40.9	2.3	2.8	9.36	0.81	0.14	98.96	0.409
PCD-21	0.70	94.2	1065	1800	8	13.2	12.9	0.93	0.3	-	33	60	2.9	3.7	-	2.8	2.3	5.81	-	-	-	0.492
-23	|	|	1224	|	32	11.4	11.3	0.96	|	-	|	490	4.1	4.1	47.1	4.5	4.3	10.69	0.71	0.13	98.57	0.471
-24	|	|	1263	|	55	11.2	11.1	1.00	|	-	|	655	4.8	4.4	50.9	3.5	4.0	10.65	0.79	0.14	97.65	0.509
-25	↓	↓	1274	↓	87	11.2	11.0	0.95	↓	-	↓	370	4.4	5.0	45.9	5.1	2.6	10.02	0.76	0.17	96.38	0.459
PCD-32	0.96	117.0	1278	1800	8	11.8	11.8	0.90	0.3	-	33	95	7.2	7.3	33.3	7.4	7.1	19.00	0.58	0.18	98.17	0.333
-33	|	|	1347	|	29	11.9	11.8	0.99	|	-	|	920	8.1	7.5	48.5	1.2	1.0	12.39	0.77	0.39	96.62	0.435
-34	|	|	1263	|	57	11.0	11.0	0.98	|	-	|	965	8.6	8.4	47.3	0.5	0.5	11.05	0.76	0.14	97.37	0.473
-35	↓	↓	1384	↓	91	11.6	11.6	0.95	↓	-	↓	780	7.9	8.2	45.4	1.1	0.5	12.67	0.76	0.48	98.59	0.454
PCD-61	1.02	84.7	1293	1500	72	11.5	11.5	0.91	0.15	-	16	>10	7.4	6.7	43.9	1.6	1.2	11.99	0.76	0.25	93 32	0.439
-62	|	|	1412	|	41	11.5	11.5	0.95	|	-	16	690	7.3	8.6	45.5	1.1	0.7	12.61	0.75	0.56	98.97	0.455
-63	|	|	1348	|	24	14.9	14.9	0.78	↓	-	16	935	6.5	6.0	38.0	0.7	0.6	12.41	0.77	0.40	98.47	0.380
-64	|	|	1424	|	12	11.7	11.5	0.92	0.3	-	33	470	9.8	10.4	24.9	9.8	11.4	29.25	0.42	0.57	99.80	0.249
-65	↓	↓	1369	↓	0	-	-	0.54	0.15	0.3	952	45	6.6	4.6	16.9	4.5	6.4	29.09	0.49	0.39	99.63	0.169
PCD-81	1.04	120.1	1419	1200	42	11.2	11.3	1.00	0.15	-	16	320	8.4	10.6	29.8	8.7	14.8	28.69	0.47	0.57	99.51	0.298
-82	|	|	1275	|	12	19.1	18.7	0.70	↓	-	16	40	2.1	3.0	35.5	3.0	2.5	9.02	0.80	0.18	97.60	0.355
-83	|	|	1351	|	11	12.3	12.2	0.86	0.3	-	33	80	6.7	6.4	34.8	5.4	6.0	18.91	0.64	0.40	97.86	0.348
-84	|	|	1418	|	29	11.5	11.3	0.97	0.15	-	16	980	7.2	8.0	48.7	0.2	0.2	11.39	0.79	0.55	97.48	0.487
-85	|	|	1397	|	57	11.5	11.5	0.94	|	-	16	1125	8.1	7.5	45.6	0.9	0.5	12.79	0.77	0.49	96.64	0.456
-89	↓	↓	1397	↓	17	11.2	11.2	0.75	↓	0.3	720	>950	7.2	8.8	20.5	8.2	8.4	27.11	0.43	0.51	99.80	0.205
PCD-101	0.82	75.8	1271	900	12	12.7	12.8	0.96	0.3	-	33	700	5.4	7.6	39.5	6.0	6.6	15.06	0.65	0.16	91.86	0.395
-103	|	|	1305	|	28	11.3	11.2	0.96	|	-	|	650	7.5	9.8	44.0	1.6	0.8	11.33	0.72	0.24	85.52	0.440
-104	|	|	1421	|	51	11.6	11.5	0.98	|	-	|	460	8.3	10.5	44.2	1.4	0.8	13.67	0.71	0.54	95.40	0.442
-105	↓	↓	1422	↓	87	11.3	11.2	0.97	↓	-	↓	190	7.9	9.8	46.2	0.5	0.4	12.56	0.75	0.54	95.03	0.462
PCD-111	-	-	1404	1500	0	-	-	0.95	-	0.15	952	335	11.5	14.1	15.1	14.1	14.8	34.54	0.25	0.51	99.88	0.151
PCD-124	0.56	98.2	1483	600	14	12.5	12.5	0.96	0.15	-	16	415	9.3	13.0	21.9	12.5	12.0	29.45	0.36	0.60	95.30	0.219
-125	|	|	1489	|	15	11.2	11.3	0.81	-	0.15	730	245	7.9	10.8	19.7	10.6	8.3	25.43	0.38	0.61	99.68	0.197
-120	|	|	1478	|	0	17.0	-	0.73	-	0.15	952	35	5.4	8.2	23.2	7.5	6.4	23.02	0.50	0.70	99.73	0.232
-122	↓	↓	1270	↓	74	17.1	16.8	0.75	0.3	-	33	35	4.2	4.3	40.2	0.5	0.2	7.46	0.84	0.16	89.04	0.402
PCD-131	0.78	82.7	1401	420	8	12.4	12.3	0.87	0.3	-	33	70	6.0	6.7	34.6	5.9	6.8	18.96	0.62	0.45	90.30	0.346
-132	|	|	1236	|	10	14.5	14.3	0.80	|	-	|	50	1.7	4.7	38.0	6.0	1.8	6.38	0.75	0.12	96.21	0.380
-133	|	|	1448	|	31	12.4	12.2	0.82	|	-	|	-	5.1	7.2	30.8	6.1	6.9	20.10	0.59	0.61	96.55	0.308
134	↓	↓	1398	↓	118	11.2	11.2	0.95	↓	-	↓	-	6.1	7.1	48.2	1.0	0.4	9.92	0.80	0.39	79.57	0.482
BSF-435	1.05	102.6	1278	5400	12	12.0	12.1	0.93	0.3	-	33	110	4.3	6.4	38.3	8.5	4.9	13.78	0.65	0.19	99.84	0.383
-434	1.05	102.4	1348	5400	119	11.1	11.2	0.97	0.3	-	33	60	6.9	10.0	32.8	9.8	7.6	20.63	0.53	0.33	99.62	0.328
-524	0.83	0.6	1353	4500	24	17.4	17.3	0.58	0.1	0.3	932	310	4.3	4.2	22.9	5.4	2.9	17.34	0.62	0.36	99.52	0.229
-465	0.57	0.4	1238	5400	65	11.3	11.2	0.98	0.3	-	33	-	2.9	5.4	54.0	0.7	0.7	5.42	0.87	0.13	95.74	0.540
-520	0.83	0.6	1353	4500	0	17.9	17.8	0.50	-	0.3	942	955	5.2	6.2	11.8	6.4	6.0	29.62	0.37	0.41	99.79	0.118
-471	|	19.2	1333	2100	102	11.0	11.0	1.00	0.3	-	33	518	4.2	5.4	54.4	0.5	1.1	7.83	0.85	0.32	96.66	0.544
-474	↓	19.2	1273	2100	71	11.1	11.1	0.94	0.3	-	33	1026	2.9	8.0	42.8	2.0	7.8	13.97	0.72	0.17	97.49	0.428
-489	0.32	12.9	1328	7200	51	12.7	11.4	0.59	0.15	0.3	742	1363	8.2	1.5	10.7	1.9	28.6	64.39	0.28	0.36	99.88	0.107
-499	0.95	7.8	1313	7805	15	13.7	14.4	0.81	0.15	0.3	720	1018	13.4	6.1	10.2	7.5	30.1	58.09	0.20	0.36	99.83	0.102
-498	0.95	7.8	1373	7805	16	13.4	13.0	0.91	0.3	-	33	1875	13.6	6.0	10.3	7.4	30.3	58.36	0.20	0.36	99.83	0.103
BSF-501	0.79	62.8	1373	3200	76	11.8	12.1	0.91	0.3	-	33	1875	3.6	4.0	45.0	2.9	5.4	13.24	0.78	0.38	99.49	0.450
-504	↓	↓	1353	↓	41	12.2	12.2	0.90	|	-	|	1880	4.6	6.3	38.5	5.8	6.0	16.16	0.67	0.35	99.63	0.385
-505	|	|	1298	|	10	15.5	15.5	0.72	|	-	|	50	2.9	4.8	32.6	5.3	1.7	10.52	0.71	0.24	99.69	0.326
-511	0.81	112.3	1323	3600	67	13.2	12.9	0.80	|	-	|	752	2.0	3.4	39.8	4.2	3.7	10.48	0.78	0.30	99.56	0.398
-514	|	|	1253	|	30	12.6	12.5	0.87	|	-	|	1328	2.9	5.4	40.8	5.1	3.4	10.16	0.74	0 13	99.86	0.408
-515	↓	↓	1383	↓	24	12.2	12.2	0.94	|	-	|	126	8.2	7.0	35.5	5.7	9.6	23.64	0.60	0.41	99.55	0.355
-552	-	66.8	1368	1960	7	-	-	-	↓	-	↓	869	-	-	-	-	-	-	-	-	-	-
-562	0.21	0.5	1423	1800	0	13.2	13.3	0.71	-	0.03	920	205	9.2	11.5	10.2	11.4	9.5	34.80	0.23	0.57	99.79	0.102
-574	0.38	0.5	1423	2700	0	15.2	15.0	0.79	-	|	952	440	13.3	11.2	10.8	11.1	13.0	41.13	0.22	0.59	99.78	0.108
-588	1.02	68.2	1393	1980	33	12.6	12.7	0.70	-	↓	720	530	10.6	10.8	10.2	9.9	10.8	37.99	0.23	0.51	99.82	0.102
-581	1.02	68.2	1413	1980	102	11.0	11.0	0.92	0.3	-	33	565	12.4	15.0	30.1	5.0	1.0	20.83	0.51	0.57	99.73	0.301
-591	0.89	64.0	1398	960	101	12.8	12.7	0.94	|	-	|	1765	7.4	7.4	47.3	0.1	0.1	11.32	0.79	0.48	94.03	0.473
-592	|	|	1453	|	87	13.4	13.2	0.95	|	-	|	2015	5.9	6.8	49.4	0.1	0.1	10.10	0.82	0.59	97.32	0.494
-593	|	|	1418	|	50	15.0	14.9	0.73	↓	-	↓	1265	8	7.0	33.0	4.0	2.3	10.86	0.73	0.55	99.46	0.330
-599	↓	↓	1463	↓	22	11.7	11.7	0.72	-	0.03	720	490	8.2	10.6	13.4	11.0	8.2	31.44	0.29	0.60	99.76	0.134

TABLE III.1 (Contd.)

Test No.	ϵ_θ^{MAX}	BOA, mm^2	Temp. K	t, s	Z_{BF}, mm	D_1, mm	D_2, mm	WTR	I_S, J	I_F, J	FMC	C_H, wt. ppm	ζ_{ox}^{o}, 10^{-2} mm	ζ_{α}^{o}, 10^{-2} mm	ζ_{β}, 10^{-2} mm	ζ^{I}, 10^{-2} mm	ζ_{ox}^{I}, 10^{-2} mm	ECR, %	F_M	C_β^{CEN} wt %	FBS, %	$I_{0.7}$, mm
BSF-611	0.89	76.1	1353	1800	26	11.0	11.1	0.89	0.09	0.12	720	125	11.4	11.4	16.2	13.1	12.6	32.92	0.29	0.36	99.84	0.162
-613	0.89	76.1	1403	1800	32	11.1	11.2	0.93	0.09	0.12	720	60	11.3	14.1	15.6	14.5	11.8	31.98	0.26	0.43	99.89	0.156
-622	0.23	6.0	1398	2400	0	12.1	12.2	1.00	0.03	-	942	330	11.5	14.0	11.7	11.3	11.4	35.90	0.23	0.42	99.85	0.117
-631	1.04	132.1	1396	3000	83	11.1	11.2	0.81	0.03	-	752	500	14.0	16.2	19.8	17.0	2.3	24.63	0.31	0.42	99.87	0.198
-651	0.67	4.2	1473	780	26	-	-	0.92	0.3	-	33	450	10.9	14.7	34.1	2.1	1.0	18.70	0.58	0.58	97.66	0.341
-652	↓	↓	1507	↓	28	-	-	0.68	0.12	0.3	932	500	8.8	9.3	12.9	9.8	8.4	34.34	0.30	0.67	99.84	0.129
-653			1393		54	-	-	0.71	0.3	-	33	805	6.8	6.8	33.6	0.1	0.1	13.40	0.75	0.41	97.04	0.336
-672	0.79	134.1	1370	900	63	10.9	10.9	0.95	0.3	-	33	700	9.5	13.5	37.4	2.9	0.9	15.96	0.62	0.37	95.79	0.374
-679			1471		26	11.1	11.1	0.99	0.15	0.3	720	230	10.2	12.6	20.2	14.2	14.3	32.37	0.32	0.60	99.82	0.202
-671	↓	↓	1423	↓	77	10.9	10.9	0.96	0.3	-	33	615	9.4	13.0	36.6	5.0	0.2	16.25	0.60	0.50	98.35	0.366
-691	0.67	0.8	1473	300	66	11.1	11.1	1.00	0.3	-	33	235	7.0	8.0	55.5	0.4	0.3	10.33	0.81	0.53	78.23	0.555
BSF-769	0.04	0.7	1473	1080	59	11.0	11.0	0.85	0.12	0.15	732	985	8.7	12.4	29.8	6.2	0.1	17.33	0.55	0.65	99.72	0.298
-779	0.82	75.4	↓	1080	92	10.9	10.9	0.87	0.15	0.3	721	770	10.1	15.6	29.2	3.8	0.1	18.63	0.53	0.65	99.59	0.292
-783	0.76	0.5	↓	1380	68	11.0	11.0	0.97	0.3	-	33	680	12.8	17.5	35.5	0.1	0.1	19.34	0.58	0.60	99.41	0.355
BSF-821	0.81	0.8	1513	600	72	11.0	11.0	1.00	0.3	-	33	-	11.5	14.3	42.8	1.8	0.5	16.95	0.64	0.70	94.94	0.227
-835	0.64	90.2	1398		49	12.7	12.5	0.94		-		735	7.9	9.9	44.8	0.1	0.1	11.89	0.75	0.43	86.97	0.448
-832			1423		4	16.2	17.3	0.90		-		30	7.8	17.6	21.7	8.0	7.7	23.78	0.38	0.56	97.76	0.217
-831	↓	↓	1513	↓	24	11.3	11.1	0.95	0.06	0.12	721	280	11.1	13.6	16.8	13.3	15.2	35.32	0.28	0.69	99.74	0.168
-859	0.69	52.5	1523	↓	17	12.3	12.2	0.74	-	0.03	730	220	10.0	13.6	10.4	9.1	11.8	37.98	0.22	0.70	99.90	0.104
-872	0.85	78.4		540	87	10.9	10.9	1.00	0.3	-	33	255	13.3	12.0	39.4	3.4	0.5	19.47	0.62	0.68	96.51	0.394
-873	0.85	78.4	↓	540	64	11.6	11.5	0.92	0.3	-	33	220	11.1	13.8	33.5	3.4	0.7	19.25	0.57	0.69	97.83	0.335
BSF-939	0.84	57.6	1573	300	0	15.6	17.8	0.58	-	0.03	920	150	6.9	10.1	10.2	8.6	6.9	32.46	0.27	0.81	99.85	0.000
-962	1.02	108.4	1273	3000	49	12.2	12.1	0.94	0.3	-	33	40	7.2	8.5	33.0	8.2	8.0	19.82	0.56	0.18	99.45	0.330
-972	0.38	0.4		2400	19	12.0	12.0	1.00		-		-	6.3	6.1	44.5	5.5	7.6	16.26	0.68	0.18	97.79	0.445
-982	1.06	84.8		2400	60	11.3	11.3	0.97		-		545	6.6	6.0	41.9	5.7	5.8	15.64	0.68	0.18	98.20	0.419
-995	1.02	84.6	↓	1800	44	12.7	12.5	0.91	↓	-	↓	830	5.0	4.9	45.4	3.2	1.7	9.77	0.79	0.17	96.43	0.454
BSF-1005	0.94	0.6	1273	1800	39	15.5	15.3	0.78	0.3	-	33	-	2.2	2.6	40.0	3.2	3.2	9.25	0.81	0.18	98.59	0.400
-1012	1.05	234.4	1273	1800	18	12.4	12.2	0.87	0.3	-	33	45	5.0	4.8	39.9	4.0	5.3	14.41	0.72	0.18	97.68	0.399
-1035	0.48	185.0	1573	240	16	10.9	10.9	0.96	0.06	0.12	720	562	10.1	16.0	17.5	15.6	8.4	28.23	0.29	0.83	98.80	0.000
-1076	0.62	41.3	1563	300	52	11.7	11.7	0.98	0.3	-	33	805	9.3	12.9	43.3	0.2	0.2	15.08	0.69	0.73	91.59	0.000
-1096	0.72	64.0	1573	240	43	12.7	12.6	0.86	0.3	-	33	990	7.2	9.6	40.5	0.1	0.1	13.68	0.74	0.76	93.20	0.000
BSF-1112	0.84	190.0	1583	210	0	-	-	0.57	-	0.03	952	40	5.3	5.6	19.1	4.8	5.0	24.96	0.53	0.85	99.69	0.000
-1124	0.66	121.4	1573	210	10	12.6	12.6	0.78	0.06	0.12	732	85	7.7	11.4	14.1	13.7	8.0	29.32	0.29	0.83	99.57	0.000
-1184	0.72	48.6	1598	120	78	11.4	11.5	0.92	0.3	-	33	320	7.2	9.6	44.2	0.1	0.1	12.68	0.75	0.67	78.98	0.256
-1183			1613		103	11.5	11.6	0.93	0.15	0.3	732	285	7.0	9.3	43.1	1.9	0.2	13.19	0.73	0.79	83.19	0.000
-1186	↓	↓	1623	↓	9	14.7	14.9	0.90	0.15	0.3	732	45	6.3	8.6	31.9	8.4	7.0	21.62	0.56	0.81	92.33	0.000
-1214	0.68	70.0	1643	150	19	11.5	11.5	0.94	0.3	-	33	540	7.1	10.0	44.9	0.1	0.1	13.09	0.75	0.88	88.25	0.000
-1223	0.81	74.5	1623	150	0	-	-	0.77	-	0.03	952	45	10.1	12.6	10.2	13.2	9.8	35.46	0.21	0.95	99.68	0.000
-1239	0.39	70.5	1633	90	0	-	-	0.76	0.06	0.09	920	160	6.2	10.1	19.0	11.0	6.2	25.04	0.40	0.95	96.68	0.000
-1249	0.59	42.0	1623	90	0	15.5	17.5	0.66	0.03	0.06	932	135	6.4	10.2	12.8	10.4	6.8	29.19	0.31	0.95	98.74	0.000
-1301	0.44	0.8	1653	47	129	11.2	11.2	0.96	0.15	0.3	722	190	11.6	19.5	33.6	0.1	0.1	17.94	0.55	0.60	63.65	0.215
-1302	0.44	0.8	1663	47	108	11.3	11.4	0.96	-	0.03	720	325	15.6	22.3	28.1	0.2	0.1	22.62	0.46	0.65	69.65	0.166
-1314	0.46	44.2	1673	30	0	15.8	18.0	0.70	-	0.05	951	380	6.5	10.2	14.4	11.4	6.3	27.12	0.33	0.98	91.51	0.000
-1363	0.50	45.8	1673	20	0	16.4	15.8	0.79	-	0.03	942	55	5.8	8.1	25.3	7.8	8.4	24.39	0.50	0.72	71.42	0.000
-1379	0.72	114.0	1673	40	0	20.2	19.0	0.63	0.12	0.15	941	435	5.1	8.9	16.1	8.1	5.4	25.14	0.40	0.96	90.76	0.000
BSF-261	0.87	128.4	1243	8100	26	11.2	11.1	1.00	0.03	0.15	720	2128	28.5	9.2	11.3	9.4	34.1	59.13	0.16	0.13	99.99	11.3
-481	0.32	12.9	1303	7200	47	11.2	11.3	0.98	0.3	-	33	1920	3.4	5.5	47.5	2.6	7.8	13.36	0.76	0.29	99.58	47.5
-483	0.32	12.9	1295	7200	61	11.9	11.8	0.93	0.3	-	33	1390	3.5	5.3	40.1	7.9	2.6	14.02	0.68	0.28	99.31	40.1
-480	0.32	12.9	1253	7200	14	11.4	11.5	0.94	0.3	-	33	2120	2.8	5.0	34.2	1.4	18.3	25.47	0.63	0.14	99.96	34.2
-1033	0.48	185.0	1543	240	13	12.0	12.1	0.93	0.03	0.15	730	1220	10.4	15.2	11.7	19.5	10.5	31.41	0.18	0.80	99.44	0.000
-1035	0.48	185.0	1573	240	15	11.8	11.8	0.96	0.03	0.15	730	1305	10.1	16.0	17.5	15.6	8.4	28.23	0.29	0.84	98.80	0.000

TABLE III.1 (Contd.)

[a] Impact velocity of ~1.7 m/s at 300 K.

[b] Definition of symbols.

ε_θ^{MAX} = maximum circumferential strain of ballooned cladding.

BOA = burst opening area; values of $\lesssim 10$ mm^2 are indicative of a pinhole rupture induced by a thermocouple spot weld.

Temp. = maximum isothermal oxidation temperature.

t = time at the isothermal oxidation temperature.

Z_{BF} = axial distance between the end of the burst opening and the point of impact.

D_1 = cladding diameter at the location of impact, parallel to the applied load.

D_2 = cladding diameter at the location of impact, perpendicular to the applied load.

WTR = wall-thickness ratio, i.e., ratio of the wall thickness immediately after rupture (i.e., before isothermal oxidation) to the original wall thickness.

I_S = impact energy that the cladding has survived at 300 K.

I_F = impact energy at which the cladding has failed at 300 K.

FMC = code for the failure mode of the cladding by impact: 16 and 33 denote cladding intact after impact at an energy of 0.15 and 0.3 J, respectively; 7XY and 9XY denote impact failure in a nonballooned or ballooned region of the tube, respectively, where X signifies the number of cladding fragments (X = 5 denotes ≥ 5) and Y indicates the crack orientation, e.g., predominantly circumferential, 0; predominantly axial, 1; and mixed-mode, 2.

C_H = hydrogen concentration.

ζ_{ox}^{O} = outer-diameter oxide-layer thickness.

ζ_{α}^{O} = outer-diameter α-layer thickness.

ζ_{β} = β-layer thickness.

ζ_{α}^{I} = inner-diameter α-layer thickness.

ζ_{ox}^{I} = inner-diameter oxide-layer thickness.

ECR = equivalent cladding reacted.

F_W = fractional thickness of the transformed β layer based on the original wall thickness.

C_β^{CEN} = oxygen concentration at the centerline of the β layer.

FBS = fractional saturation of the β phase with oxygen.

$L_{0.7}$ = thickness of β-phase layer containing $\lesssim 0.7$ wt % oxygen.

TABLE III.2. Summary of Results[a] from Diametral Tube-compression Tests[b] on Ruptured Zircaloy-4 Cladding That Survived Thermal-shock and Impact[c] Loads

Test No.	Temp., K	t, s	D_1, mm	D_2, mm	WTR.	I_g, J	I_F, J	L_m, kg	d_E, mm	d_M^o, mm	d_M^F, mm	d_M^C, mm	d_I^M, mm	d_T, mm	d_{PCD}, mm	ϵ_*^M, J	ϵ^T, J	C_H, wt. ppm	ζ_{ox}^o, 10^{-2} mm	ζ_β^o, 10^{-2} mm	ζ_β, 10^{-2} mm	ζ_β^I, 10^{-2} mm	ζ_{ox}^I, 10^{-2} mm	ECR, %	F_W	C_β^{CEN}, wt %	FBS, %	$L_{0.7}$, mm
PCD-10	~1123[d]	1800	19.61		0.680	0.15–0.3	-	131.7	1.26	2.31	-	5.81	3.57	-	9.38	2.631	-	55	2.3	3.4	-	2.4	2.0	6.80	-	-	-	0.349
-13	1270	↓	12.50	12.35	0.85	↓	-	82.8	0.35	0.98	-	0.76	1.45	-	2.21	0.716	-	535	5.0	4.8	38.6	4.4	5.0	14.40	0.71	0.18	97.94	0.386
-12	1278		11.80	11.75	0.97		-	74.8	0.28	1.29	-	0.06	1.67	-	1.73	0.516	-	795	5.2	4.4	48.9	1.2	5.7	13.06	0.80	0.17	95.66	0.489
-11	1273		11.70	11.50	0.97		-	215.0	0.40	0.54	-	0.98	1.16	-	2.14	0.921	-	335	5.8	5.5	50.8	1.3	0.2	8.14	0.83	0.17	94.78	0.508
PCD-20	~1023	1800	18.50	-	0.69	0.15–0.3	-	375.0	0.76	7.18	-	0.10	7.94	-	8.04	14.630	-	50	1.5	1.8	-	1.5	1.6	4.90	-	-	-	0.388
-22	~1073		14.65	14.05	0.86		-	365.2	0.79	1.40	-	0.00	-	-	2.29	2.000	-	55	1.6	3.2	-	1.8	1.6	4.10	-	-	-	0.478
-23	1224		11.40	11.35	0.96		-	162.2	0.36	0.36	-	0.16	0.82	-	0.98	0.565	-	490	4.1	4.1	47.1	4.5	4.3	10.69	0.71	0.13	98.57	0.471
-24	1263		11.20	11.11	1.00		-	288.0	0.31	0.48	-	0.00	-	-	0.83	0.636	-	655	4.8	4.4	50.9	3.5	4.0	10.65	0.79	0.14	97.65	0.509
-25	1274	↓	11.20	11.10	0.95	↓	-	320.0	0.34	0.46	-	0.00	-	-	0.88	0.853	-	370	4.4	5.0	45.9	5.1	2.6	10.02	0.76	0.17	96.38	0.459
PCD-30	~1253	1800	21.4	-	0.77	0.15–0.3	-	126.5	0.32	4.66	-	5.72	5.16	-	10.88	3.340	-	60	6.4	7.5	28.9	5.3	4.9	17.64	0.59	0.13	99.61	0.289
-33	1347		11.95	11.85	0.99		-	52.5	0.19	0.28	-	0.56	0.50	-	1.06	0.141	-	920	8.1	7.5	48.5	1.2	1.0	12.39	0.77	0.39	96.62	0.485
-35	1384	↓	11.65	11.65	0.95	↓	-	51.5	0.24	0.31	-	0.51	0.31	-	0.82	0.745	-	780	7.9	8.2	45.4	1.1	0.5	12.67	0.76	0.48	98.59	0.454
PCD-42	1339	1800	11.65	11.50	0.91	-	-	85.1	0.29	0.60	-	0.00	-	-	0.89	0.413	-	735	8.5	6.8	43.6	1.6	0.9	13.38	0.75	0.35	96.97	0.436
-41	1293		11.45	11.35	0.96	-	-	30.7	0.28	0.25	-	0.10	0.58	-	0.68	0.112	-	655	8.9	9.0	43.8	1.7	1.1	13.15	0.72	0.25	94.18	0.438
-49	1423		11.40	11.35	0.94	-	T.S.[e]	10.5	0.06	0.07	0.56	-	0.13	0.69	-	0.008	0.042	1895	9.2	16.4	8.8	10.3	28.9	47.40	0.15	0.57	98.89	0.088
-43	~1373	↓	11.25	11.25	1.00	-	-	48.4	0.20	0.14	-	0.34	0.36	-	0.70	0.089	-	1090	9.2	8.3	40.8	1.0	0.2	12.73	0.76	0.38	97.41	0.480
PCD-50	1303	1842	19.00	-	0.65	-	-	26.3	0.31	0.06	3.52	-	0.38	3.90	-	0.048	0.513	80	6.9	5.9	20.3	6.3	7.2	26.02	0.49	0.29	99.81	0.203
-53	1353		12.30	12.25	0.91	-	-	42.0	0.21	0.61	-	0.83	0.85	-	1.68	0.236	-	815	7.8	6.4	38.5	3.8	6.8	19.75	0.66	0.41	98.96	0.385
-51	1269		11.85	11.75	0.95	-	-	149.2	0.34	0.97	-	0.05	1.35	-	1.40	0.478	-	605	5.3	6.5	48.9	1.1	0.6	8.27	0.81	0.17	95.27	0.489
-52	1287	↓	11.60	11.45	1.00	-	-	131.9	0.38	0.17	-	0.44	0.57	-	1.01	0.118	-	70	6.2	5.6	53.2	1.2	0.8	9.12	0.82	0.25	92.75	0.532
PCD-63	1368	1500	14.90	14.90	0.78	0.15	-	52.6	0.39	0.25	-	3.55	0.67	-	4.22	0.192	-	935	6.5	6.0	38.0	0.7	0.6	12.41	0.77	0.40	98.47	0.380
-62	1412	-	11.55	11.50	0.95	↓	-	60.0	0.34	0.50	-	0.00	-	-	0.87	0.285	-	690	7.3	8.6	45.5	1.1	0.7	12.61	0.75	0.56	98.97	0.455
-61	1293	↓	11.55	11.50	0.91	↓	-	80.8	0.37	0.33	-	0.06	0.71	-	0.77	0.302	-	510	7.4	6.7	43.9	1.6	1.2	11.99	0.76	0.25	93.32	0.439
PCD-80	1263	1200	22.65	-	0.54	0.15	-	146.5	1.08	2.42	-	8.26	3.55	-	11.81	3.010	-	55	1.8	1.8	28.5	1.8	1.6	8.30	0.83	0.14	99.64	0.285
-85	1397	↓	11.55	11.50	0.94	↓	-	71.9	0.25	0.44	-	0.12	0.73	-	0.85	0.245	-	1125	8.1	7.5	45.6	0.9	0.5	12.79	0.77	0.49	96.84	0.456
PCD-100	~1223	900	19.9	-	0.62	0.15–0.3	-	59.2	0.36	1.00	5.66	-	1.37	7.03	-	0.396	1.801	50	3.1	4.0	27.7	3.4	3.3	12.65	0.71	0.13	99.01	0.277
-105	1422		11.30	11.25	0.97		-	141.8	0.26	0.26	-	0.12	0.64	-	0.76	0.510	-	190	7.9	9.8	46.2	0.5	0.4	12.56	0.75	0.34	95.03	0.462
-104	1421	↓	11.65	11.50	0.98	↓	-	90.4	0.42	0.26	-	0.10	0.73	-	0.83	0.305	-	460	8.3	10.5	44.2	1.4	0.8	13.67	0.71	0.34	95.40	0.442
PCD-113	1358	1500	12.10	12.10	0.98	-	-	106.1	0.43	0.78	-	0.68	1.21	-	1.89	0.765	-	515	7.7	7.9	47.3	1.6	0.7	11.93	0.76	0.39	95.29	0.473
-112	1393		11.70	11.50	1.00	-	-	39.0	0.14	1.00	-	0.12	1.14	-	1.26	0.196	-	1060	8.5	8.4	47.5	1.6	0.5	12.90	0.75	0.50	97.51	0.475
-115	1385	↓	11.25	11.20	0.96	-	-	127.0	0.34	0.41	-	0.00	-	-	0.75	0.465	-	50	7.2	9.2	46.5	0.7	0.3	11.58	0.76	0.47	97.26	0.465
PCD-120	~1478	600	17.0	-	0.60	-	0.15	9.3	1.20	0.63	4.07	-	1.83	5.90	-	0.088	0.222	35	5.3	6.4	18.6	5.7	6.4	26.09	0.49	0.70	99.68	0.186
-122	1270		17.0	16.85	0.75	0.15	-	50.7	0.94	0.93	-	4.75	1.93	-	6.68	0.366	-	435	4.2	4.3	40.2	0.5	0.2	7.46	0.84	0.16	89.04	0.402
-124	1483	↓	12.50	12.50	0.96	0.15	-	17.1	0.27	0.34	1.73	-	0.61	2.34	-	0.051	0.279	415	9.3	13.0	21.9	12.5	12.0	29.45	0.36	0.70	99.38	0.218
PCD-130	1323	420	19.50	-	0.60	0.15–0.3	-	121.8	0.76	0.91	3.88	-	1.71	5.59	-	1.073	2.562	35	2.0	4.5	27.8	3.9	1.4	7.86	0.72	0.13	97.45	0.278
-133	1448		12.40	12.25	0.82		-	66.3	0.32	0.80	-	0.92	1.12	-	2.04	0.536	-	-	5.1	7.2	30.8	6.1	6.9	20.10	0.59	0.61	96.55	0.308
-135	1393	↓	12.00	12.00	0.93	↓	-	118.2	0.45	0.61	-	0.12	1.16	-	1.28	0.765	-	-	5.7	6.5	46.9	1.4	0.8	10.18	0.80	0.40	81.17	0.469

[a] Symbols are the same as in Table III.1 with the following additions.

L_m = maximum load from diametral tube-compression test.

d_E = elastic deflection from diametral tube-compression test (deflection BC in Figs. III.2 and III.3).

d_M^o = plastic deflection to the point of maximum load (deflection CD in Fig. III.2).

d_M^F = deflection from the point of maximum load to fragmentation (deflection DE in Fig. III.3).

d_M^C = deflection from the point of maximum load to cladding-pellet contact (deflection DE in Fig. III.2).

d_I^M = total deflection to maximum load (deflection AD in Fig. III.2 or III.3).

d_T = total deflection to fragmentation (deflection BE in Fig. III.3).

d_{PCD} = total deflection to cladding-pellet contact (deflection AE in Fig. III.2).

ϵ_*^M = integrated energy from load-deflection curve to maximum load in the tube-compression test.

ϵ^T = integrated energy from load-deflection curve to fragmentation in the tube-compression test.

[b] Compression rate of 0.043 mm/s at 300 K.

[c] Impact velocity of ~1.7 m/s at 300 K.

[d] Estimated temperature.

[e] Cladding failed by thermal shock upon bottom-flooding with water after cooling to ~1100 K at a rate of ~5 K/s.

TABLE III.3. Tensile Properties[a] of Six Zircaloy-4 Cladding Specimens after Rupture and Oxidation in Steam[b]

Test No.	Temp., K	t, s	BOA, mm^2	Z_{BF}, mm	ϵ_D	WTR	L_m, kg	ℓ, mm	ϵ^T, J	C_H, wt ppm	ζ^o_{ox}, 10^{-2} mm	ζ^o_α, 10^{-2} mm	ζ_β, 10^{-2} mm	ζ^I_α, 10^{-2} mm	ζ^I_{ox}, 10^{-2} mm	ECR, %	C^{CEN}, wt %
CH-2[c]	1273	1800	46.1	14.4	0.102	0.99	290.2	0.23[d]	3.240	-	6.6	2.6	49.8	2.5	5.3	13.83	0.17
BSF-530	1189	1800	325.6	0.0	1.290	0.54	-	-	-	55	1.0	1.9	29.0	1.9	1.0	5.78	0.13
-534	~1270	1800	-	37.1	0.142	0.92	-	-	-	242	1.6	8.3	40.8	7.5	1.5	6.96	0.17
-539	1422	1800	-	54.2	0.034	1.00	404.2	1.75[d]	3.491	642	1.9	9.6	40.2	8.2	9.5	16.82	0.47
BSF-540	894	3600	164.2	0.0	0.950	0.64	496.5	3.43[e]	6.810	50	2.0	19.0	0.0	19.0	1.9	13.56	0.14
-541	1423	3600	-	14.9	0.143	0.80	-	-	-	41	2.7	6.5	35.5	5.8	2.4	11.84	0.47
-542	1123	3600	-	36.5	0.181	0.93	-	-	-	125	2.7	5.2	44.0	5.4	3.8	9.65	0.12
HD-20	1215	1900	38.4	0.0	0.655	0.67	182.2	1.74[e]	1.440	43	2.2	5.0	29.8	4.8	2.5	9.99	0.13
-22	1243	1900	-	9.0	0.209	0.84	-	-	-	41	2.1	3.5	43.2	4.0	2.1	7.17	0.13
-24	1203	1900	-	33.4	0.042	0.97	-	-	-	48	1.8	3.2	52.8	3.4	1.3	5.06	0.13
HD-30	1273	1800	1.7	0.0	0.321	0.83	-	-	-	134	7.4	5.5	32.2	6.0	6.4	19.65	0.18
-39	1356	1800	-	38.8	0.042	0.99	190.5	0.97[d]	0.705	1725	7.7	8.2	34.0	8.2	12.2	24.57	0.35
-34	1283	1800	-	27.0	0.081	0.94	-	-	-	24	1.8	2.7	52.2	2.6	1.8	5.72	0.17
HD-40	1248	1800	69.8	0.0	0.709	0.67	149.9	1.27[e]	0.934	31	1.6	2.1	36.0	2.1	1.7	6.80	0.13
-43	1277	1800	-	22.1	0.061	0.97	-	-	-	228	5.6	5.8	42.8	5.7	6.2	14.78	0.17
-45	1033	1800	-	28.5	0.011	0.97	-	-	-	45	1.0	30.2	0.0	30.2	1.0	8.56	0.12

[a]Test temperature and crosshead speed are 300 K and 0.043 mm/s, respectively.
[b]Definitions are the same as in Tables III.1 and III.2 with the following additions.
ϵ_D = average diametral strain due to deformation during ballooning and rupture.
L_m = maximum tensile load.
ℓ = total elongation at fracture.
[c]Test temperature 430 K, crosshead speed 0.254 mm/s.
[d]Predominantly circumferential fracture in a nonballooned region.
[e]Predominantly circumferential fracture in the ballooned region.

In comparison with the criterion for thermal-shock failure, the maximum oxidation limits in the acceptance criteria for ECCS's in LWR's (i.e., peak cladding temperature of 1477 K and total oxidation of the cladding less than 0.17 times the total cladding thickness before oxidation) are quite conservative. However, evaluation models, which are used to calculate the expected performance of the ECCS, must properly account for the extent of wall thinning due to ballooning, the axial temperature profile in the cladding, and the effects of anomalous oxidation. Otherwise, the calculated critical oxidation times to achieve the minimum allowable β-layer thickness at a given temperature will be larger than the experimental values for thermal shock and impact failure of the cladding. In general, the uncertainty in the calculated performance of the ECCS will increase as the maximum oxidation temperature increases.

References

1. Light-water-reactor Safety Research Program: Quarterly Progress Report, January-March 1979, Sec. III, "Mechanical Properties of Zircaloy," ANL-79-43, NUREG/CR-1040 (Aug 1979).

2. S. Kawasaki, T. Furuta, and H. Uezuka, "Inner Surface Oxidation of Zircaloy Cladding in a Loss-of-Coolant Accident," Sixty Water-Reactor-Safety Research Information Meeting, National Bureau of Standards, Gaithersburg, MD (Nov 6-9, 1978).

3. S. Kawasaki, "Inner Surface Oxidation of Zircaloy Cladding Under a LOCA," Japanese Atomic Energy Research Institute/German Projekt Nucleare Sicherheit/U. S. Nuclear Regulatory Commission Annual Information Exchange Meeting on Fuel Behavior Research and Modeling, Idaho Falls, ID (June 25-29, 1979).

4. H. M. Chung and T. F. Kassner, Embrittlement Criteria for Zircaloy Fuel Cladding Applicable to Accident Situations in Light-water Reactors: Summary Report, ANL-79-48 (in press).

Distribution for NUREG/CR-1164 (ANL-79-81)

Internal:

W. E. Massey
J. A. Kyger
J. R. Honekamp
H. K. Fauske
M. V. Nevitt
B. R. T. Frost
R. Avery
R. W. Weeks
M. Blander
C. E. Dickerman
L. W. Deitrich
E. E. Gruber
R. G. Palm
P. A. Lottes
R. P. Anderson
M. Ishii
R. P. Stein
R. E. Henry (7)
L. McUmber
W. Wang
F. L. Yaggee
Y. S. Cha
J. C. Leung
L. A. Neimark
R. B. Poeppel
D. Stahl
D. R. Pepalis
E. Stefanski
W. D. Jackson
Y. Y. Liu
S. M. Gehl
T. F. Kassner (23)
H. M. Chung
A. M. Garde
J. Rest (30)
A. B. Krisciunas
ANL Contract File
ANL Libraries (5)
TIS Files (6)

External:

NRC, for distribution per R2, R3, R4 (550)
DOE-TIC (2)
Manager, Chicago Operations and Regional Office, DOE
Chief, Office of Patent Counsel, DOE-CORO
President, Argonne Universities Association
Reactor Analysis and Safety Division Review Committee:
S. Baron, Burns and Roe, Inc.
J. R. Dietrich, Combustion Engineering, Inc.
W. Kerr, U. Michigan
M. Levenson, Electric Power Research Inst.
S. Levy, S. Levy, Inc.
D. Okrent, U. California, Los Angeles
N. C. Rasmussen, Massachusetts Inst. Technology
Materials Science Division Review Committee:
E. A. Aitken, General Electric Co., Sunnyvale
G. S. Ansell, Rensselaer Polytechnic Inst.
R. W. Balluffi, Massachusetts Inst. Technology
R. J. Birgeneau, Massachusetts Inst. Technology
S. L. Cooper, U. Wisconsin
C. Laird, U. Pennsylvania
M. T. Simnad, General Atomic
C. T. Tomizuka, U. Arizona
A. R. C. Westwood, Martin Marietta Labs.